From long- to short-term inter-plate coupling at the subducted Carnegie Ridge crest, offshore Central Ecuador

J-Y Collot, J-n. Proust, J-m Nocquet, C. Martillo, F. Michaud, J-f. Lebrun, Laure Schenini, S. Popescu, M-j Hernandez, G. Ratzov

JGR Solid Earth

RESEARCH ARTICLE
10.1029/2022JB024192

From Long- to Short-Term Inter-Plate Coupling at the Subducted Carnegie Ridge Crest, Offshore Central Ecuador

J.-Y. Collot[1], J.-N. Proust[2], J.-M. Nocquet[1], C. Martillo[3], F. Michaud[1,4], J.-F. Lebrun[5], L. Schenini[1], S. Popescu[6], M.-J. Hernandez[7], and G. Ratzov[1]

[1]Université Côte d'Azur, IRD, CNRS, Observatoire de la Côte d'Azur, Valbonne, France, [2]Université de Rennes, CNRS, Rennes, France, [3]Escuela Superior Politécnica del Litoral, GEMAC-FIMCM-CADS, Guayaquil, Ecuador, [4]Sorbonne Université, Institut des Sciences de la Terre, Paris, France, [5]Université des Antilles, Université de Montpellier, CNRS, Guadeloupe (FWI), Pointe à Pitre, France, [6]Geobiostratdata.Consulting, Rillieux la Pape, France, [7]Departamento de Geológica, Escuela Politécnica Nacional, Quito, Ecuador

Abstract We investigate the relationship between the long-term (Quaternary) interplate coupling and the short-term geodetically derived interseismic coupling at the Central Ecuador subduction zone. At this nonaccretionary margin, the Cabo Pasado shelf promontory and coastal area are associated with two inter-plate geodetically locked patches. The deepest patch ruptured co-seismically during the Mw7.8-2016 Pedernales earthquake, while the shallowest underwent dominantly after-slip. Marine geophysical and chronostratigraphic data allow reconstructing the Quaternary tectonic evolution of the shelf promontory and substantiating variation of the long-term inter-plate coupling that led to the geodetically locked patches. Prior to ~1.8 Ma, the outer-wedge inter-plate coupling was strong enough to activate trench-subparallel strike-slip faults. Then, between ~1.8 and 0.79 Ma, shortening and uplift affected the shelf promontory, implying a locally increased inter-plate coupling. After a short, post-0.79 Ma period of subsidence, shortening and uplift resumed denoting a high inter-plate coupling that endured up to the present. The synchronicity of the structural evolution of the shelf promontory with the subduction chronology of two reliefs of the Carnegie Ridge crest suggests that the locked patches are caused by a geometrical resistance to subduction that propagates landward causing permanent deformation. In 2016, the deepest subducted relief localized stress accumulation and high seismic slip, while the shallowest relief, which is associated with a weakened outer-wedge, prevented updip rupture propagation. Thus, at nonaccretionary margins, active outer-wedge strike-slip faults might be considered a proxy of near-trench coupling, and subducted relief a cause of plate coupling but an obstacle to the tsunami genesis when the relief is shallow.

Plain Language Summary The 2016-Ecuador earthquake ruptured a subduction fault segment previously locked for decades beneath the coastline. The rupture was arrested updip by another locked fault segment called locked patch, which instead slipped slowly. To understand the cause of the locked patches, their rupture behaviors, and whether the decadal fault locking and long-term subduction processes are related, we reconstructed the Quaternary tectonic evolution of the margin offshore Central Ecuador using geophysical data. We consider that tectonic deformation reflects the long-term inter-plate coupling, which is the ability of the fault to transfer long-term stress and strain to the margin. Prior to ~1.8 Ma, a trench-subparallel fault accommodating lateral displacement indicates a shallow plate coupling, which increased locally between ~1.8 and 0.79 Ma as shown by margin shortening. After a brief subsidence, shortening resumed, denoting a strong coupling that persisted until today in the form of the locked patches. Although many physical factors have been proposed to control plate coupling, here we find that the locked patches are caused by the subduction of two reliefs of a submarine ridge. Remarkably, in 2016, the deepest relief released high elastic strain, while the shallower relief, thrust under a weakened outer-margin, damped updip rupture propagation, impeding a significant tsunami.

Key Points:

- A trench-parallel strike-slip fault and its earthquake-controlled fault scarps substantiate a pre-1.8 Ma, outer-wedge inter-plate coupling
- From 1.8 Ma, a robust shelf uplift caused by subducted reliefs highlights a long-term coupling that led to geodetically locked patches
- The shallowest subducted relief likely impeded the generation of a major tsunami during the Mw 7.8, 2016 event

Supporting Information:

Supporting Information may be found in the online version of this article.

Correspondence to:

J.-Y. Collot,
jean-yves.collot@ird.fr

Citation:

Collot, J.-Y., Proust, J.-N., Nocquet, J.-M., Martillo, C., Michaud, F., Lebrun, J.-F., et al. (2022). From long- to short-term inter-plate coupling at the subducted Carnegie Ridge crest, offshore Central Ecuador. *Journal of Geophysical Research: Solid Earth*, *127*, e2022JB024192. https://doi.org/10.1029/2022JB024192

Received 9 FEB 2022
Accepted 27 JUL 2022

1. Introduction

In subduction zones, Global Positioning System (GPS) data have been used to demonstrate inter-seismic locked patches to correlate well with regions of high co-seismic slip (Bilek & Lay, 2018). Although major earthquakes may alter the inter-plate coupling over a decadal-scale (Philibosian et al., 2014), in many locations, subduction earthquakes have repeatedly ruptured the same fault segment as exemplified in Ecuador over the past 110 years

(Nocquet et al., 2017; Ye et al., 2016), in central Peru (Perfettini et al., 2010), and southern Chile (Moreno et al., 2010) over several centuries. These observations point to some persistence of the megathrust properties through several earthquake cycles. Paleo-seismology provides evidence of a ∼10 ka persistence of the plate coupling and barriers to megathrust rupture propagation (Goldfinger et al., 2012).

On the scale of the earthquake cycle, simple models only consider elastic rheology where inter-seismic and co-seismic stress/strain would cancel over several cycles. At longer time scales (>100 ka), irreversible anelastic deformation also occurs within the fore-arc and cumulates through time (Matsuura & Sato, 1989). Possible mechanisms are one or a combination of (a) subduction earthquakes and subsequent post-seismic deformation not relieving all of the strain accumulated during inter-seismic period, (b) plastic deformation occurring as inter-seismic stress exceeds the yield stress, and (c) damages occurring close to the plate interface as well as fore-arc folding and faulting. The fraction of the documented short-term strain converting to permanent deformation remains poorly known, with estimates ranging from less than 4%–∼10% (Allmendinger et al., 2005; Baker et al., 2013; Jolivet et al., 2020; van Dinther et al., 2013). However, regardless of the magnitude of this ratio, several studies highlight the similarity between the spatial pattern of the inter-seismic strain and that of the permanent deformation (Allmendinger et al., 2005; Béjar-Pizarro et al., 2013; Jolivet et al., 2020).

Beyond the GPS-derived inter-plate coupling that expresses the fault kinematic during the earthquake cycle (Wang & Dixon, 2004), the Coulomb wedge theory (Davis et al., 1983; Lallemand et al., 1994; Wang & Hu, 2006) indicates that the average state of convergent margin deformation over a long-time period depends, amongst other parameters, on the long-term basal friction, and varies from compressively critical to extensionally critical. Therefore, reconstructing the detailed, $\sim 10^5$–10^6-years' time-scale, structural evolution of the margin wedge can inversely provide information on the inter-plate strength that characterizes the long-term plate coupling (e.g., Saillard et al., 2017; Victor et al., 2011). Following this rationale, scrutinizing the activity of fore-arc faults that root in the megathrust can substantiate the long-term behavior of plate coupling. Mechanical models show that splay faults can transfer slip to the seafloor during megathrust events (Kame et al., 2003; Wang & Hu, 2006). Indeed, splay faults have been shown to slip co-seismically in Nankai (Yamaguchi et al., 2011) and Chili (Lieser et al., 2014), and such repeated activity has been inferred in the Arauco bay in Chili (Jara-Muñoz et al., 2017), and Alaska, where Liberty et al. (2019) suggest a millennial-scale persistence of the 1964 earthquake asperity. Similarly, ten Brink and Lin (2004) show that seismic slip on the megathrust plays a significant role in the slip of upper-plate strike-slip faults, contributing to long-term strain partitioning (Fitch, 1972).

This study combines marine geophysical data, and sedimentary cores collected offshore Central Ecuador (Figure 1) to decipher the Quaternary activity of a strike-slip fault system that roots in the megathrust (Figure 2) and extends across an inter-seismic locked patch (the Cabo Pasado [CP] patch), and a creeping barrier (Chlieh et al., 2014; Nocquet et al., 2017) (Figures 1b and 1c). Based on the lifespan of the strike-slip fault system and the subsequent detailed structural evolution of the margin wedge, we (a) estimate the Quaternary variation of the shallow megathrust coupling, (b) investigate its cause and relationship to geodetic inter-seismic coupling (ISC), as well as the reasons for the spatial distribution of seismic and aseismic slip, and (c) discuss the styles of permanent deformation associated with a change in megathrust slip mode from stick and slip (Scholz, 1998) to transient aseismic slip (Schwartz & Rokosky, 2007).

2. Geodynamic Setting, Seismicity, and Inter-Seismic Coupling

In absence of a frontal accretionary wedge (von Huene and Scholl, 1991), the convergent margin of Ecuador is considered nonaccretionary and controlled by basal erosion (Sage et al., 2006). It is underthrusted eastward by the Carnegie Ridge (CR), a 14–19 km-thick and buoyant oceanic feature (Graindorge et al., 2004; Lonsdale, 1978; Sallares et al., 2005) carried along by the Nazca plate at 4.7 cm/yr with respect to the North Andean sliver (Nocquet et al., 2014) (Figure 1a). Land-based GPS and seismological measurements have revealed that North of CP (Figure 1b), the plate interface shows strong ISC (Chlieh et al., 2014; Nocquet et al., 2014; Gombert et al., 2018) and has produced a remarkable seismic sequence that started with the great Mw 8.6–8.8, 1906 earthquake (Kelleher, 1972; Kanamori & McNally, 1982; Ye et al., 2016). Four Mw 7.7 to 8.2 earthquakes (Beck & Ruff, 1984; Mendoza & Dewey, 1984; Swenson & Beck, 1996), including the Mw 7.8, 2016 Pedernales earthquake, later broke sub-segments of the same area (Figure 1a). In contrast, south of CP, no events with Mw > 7.0–7.2 have ruptured the plate interface, and the megathrust shows low ISC (Chlieh et al., 2014; Nocquet

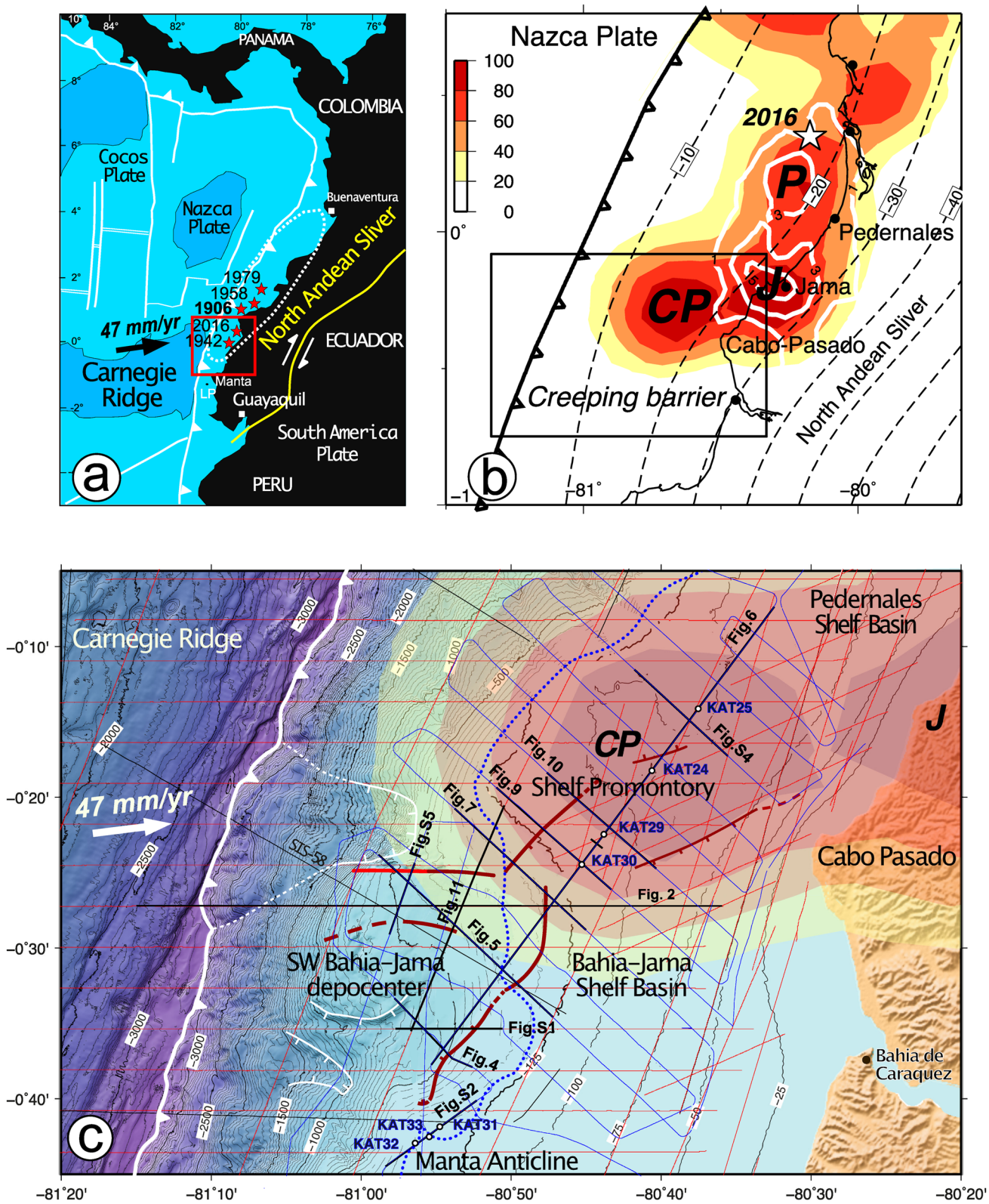
a
PANAMA
COLOMBIA
Cocos Plate
Nazca Plate
Buenaventura
North Andean Sliver
1979
1958
1906
2016
1942
47 mm/yr
ECUADOR
Carnegie Ridge
Manta
LP
Guayaquil
South America Plate
PERU
b
Nazca Plate
100
80
60
40
20
0
2016
P
CP
J
Jama
Pedernales
Cabo-Pasado
Creeping barrier
North Andean Sliver
c
Carnegie Ridge
47 mm/yr
Pedernales Shelf Basin
CP
Shelf Promontory
J
Cabo Pasado
SW Bahia–Jama depocenter
Bahia–Jama Shelf Basin
Manta Anticline
Bahia de Caraquez
KAT25
KAT24
KAT29
KAT30
KAT33
KAT31
KAT32
Fig.6
Fig.S4
Fig.10
Fig.9
Fig.7
Fig.S5
Fig.11
Fig.5
Fig. 2
Fig.S1
Fig.4
Fig.S2
STS-58

Figure 1.

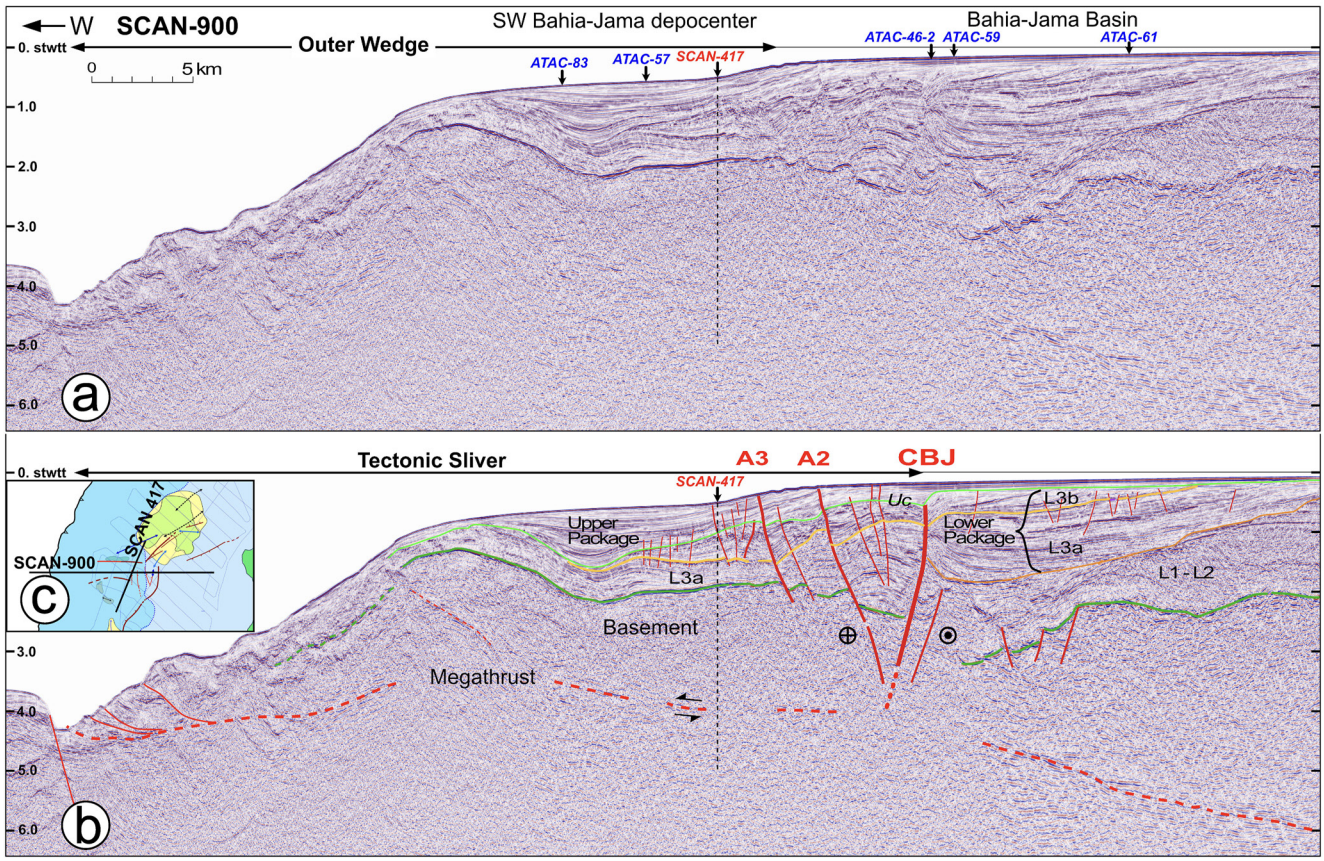

Figure 2. Deep penetrating seismic reflection SCAN line 900 across the margin wedge offshore Cabo Pasado. (a) Un-interpreted section with crossing seismic lines; (b) the line shows the outer wedge tectonic sliver, the Central Bahia Jama (CBJ) strike-slip fault segment and the megathrust; L1 and L2 units = Middle Eocene to Late Miocene, and L3a and L3b units = Pliocene to early Pleistocene (Hernandez et al., 2020); Uc (light green) is major unconformity between lower and upper packages, and outlines the CBJ paleo fault scarp. Note that faults A2 and A3 recorded extensional deformation during unit L3b deposition. Strong reflector (dark green) shows the margin basement to be faulted by the CBJ-A2 fault system, and strongly eroded beneath the SW Bahia Jama depocenter; (c) map showing line location.

et al., 2014), forming a creeping barrier (Gombert et al., 2018) that has remained persistent over the last earthquake cycles (Figure 1b). This remarkable segmentation in seismogenic behavior and ISC along strike the Ecuador margin is likely related to variations in structure and composition of the down-going plate (Agurto-Detzel et al., 2019; Collot et al., 2004; Gutscher et al., 1999; León-Ríos et al., 2021; Soto-Cordero et al., 2020; Swenson & Beck, 1996) and the Ecuadorian forearc (Collot et al., 2004; Koch et al., 2020; Lynner et al., 2020).

In 2016, the Pedernales earthquake mainly ruptured two, ~20–30-km-deep locked patches (P and J in Figure 1b) while propagating southward (Nocquet et al., 2017; Ye et al., 2016). Updip of the Jama patch (J in Figure 1b), the co-seismic rupture was arrested beneath the CP shelf promontory by the ~10–15-km-deep, 50 × 50 km CP locked patch, centered ~45 km landward from the trench. During the 30 days following the main shock, a large (60 cm) and rapid after-slip developed at this patch, coincidently with a remarkable after-shocks sequence (Agurto-Detzel et al., 2019; León-Ríos et al., 2021; Rolandone et al., 2018; Soto-Cordero et al., 2020).

Figure 1. Geodynamic setting, bathymetry, inter-seismic coupling, and location of seismic lines in the study area. (a) Geodynamic setting, red frame is location of Figure 1b in Central Ecuador where Carnegie Ridge is subducting; red stars are 1906–2016 large to great subduction earthquakes. Dash ellipse is estimated rupture zone of the Mw 8.6–8.8, 1906 earthquake (Kelleher, 1972). 47 mm/yr is convergence rate between Nazca plate and North Andean sliver (Nocquet et al., 2014). LP = La Plata Island; (b) Inter-seismic coupling map (color bar 0%–100%) with Pedernales (P), Jama (J), and Cabo Pasado (CP) locked asperities (Rolandone et al., 2018); White star is epicenter of the Mw 7.8, 2016 with white contours indicating co-seismic slip in meters. Dashed lines are estimated depth contours of the plate interface in km (Hayes et al., 2012). Black frame is location of (c). (c) Multibeam bathymetric map with contours every 50 and 25 m on the shelf. White barbed line is the subduction trench; blue dotted line is shelf edge; white lines with tick marks are slope scars; thin red lines are SCAN seismic data; thin blue lines are ATACAMES seismic and chirp data (Michaud et al., 2015); SIS-58 is SISTEUR seismic line from Collot et al. (2004); bold segments with figure numbers are the seismic sections presented in the text and supporting information; yellow-orange pattern represents CP and J locked asperities; simplified fault pattern in red (see Figure 3). KAT24 to 33 are ATACAMES coring sites.

3. Data and Methods

3.1. Multibeam Bathymetric Data

The bathymetric map (Figure 1c) is a compilation of swath bathymetry data collected during the 2005 Amadeus and Esmeraldas cruises (RV L'Atalante), using a SIMRAD EM12D multibeam system (13 kHz, 162 beams) (Collot et al., 2005). This data set was completed by higher-resolution multibeam swath data collected on the shelf using SIMRAD EM122 (12 kHz, 288 beams) and EM710 (100 kHz, 256 beams) echosounders during the 2012 Atacames cruise (RV L'Atalante) (Michaud et al., 2015). The RV L'Atalante bathymetric data were processed using the CARAIBES software (IFREMER). The whole data set allowed constructing a uniform digital elevation model with a 30-m grid spacing, using the nearest neighbor algorithm of the GMT software (Wessel & Smith, 1998).

3.2. Multi-Channel Seismic Imaging and Chirp Data

A grid of Multichannel seismic reflection data was acquired during the 2009 Scan and 2012 Atacames cruises (Figure 1c). Scan data were recorded using a 4000-in^3 (65.5 L), 20- to 80-Hz frequency air gun seismic source, and a 640-channel, 8-km-long digital streamer. Shots were fired every 25 m, providing a 160-fold coverage. Scan data were processed by SINOPEC (China Petroleum and Chemical Corporation) for PetroEcuador through classical steps (Yilmaz, 2001), including multiple elimination, spherical divergence compensation, predictive deconvolution in the Tau-P domain, prestack noise attenuation, stacking, and prestack time migration. Atacames high-resolution seismic reflection data were recorded using a 72-channels, 450-m-long digital streamer. The source array consisted of two 13/13 in^3 plus two 24/24 in^3 mini-GI (Generator-Injector) guns, providing a signal with a peak frequency at ∼130 Hz. Shots were fired at 140 bars every 25 m ensuring a nine-fold stack. The seismic lines were processed on board with the Seismic Unix software (Center of Wave Phenomena, Colorado School of Mines) for band pass filtering, spherical divergence correction (water velocity), normal moveout (NMO) velocity analysis and correction, stack and constant velocity-time migration (1,490 m/s). Sub-bottom profiler (Chirp), 1.8–5.3 kHz reflection data were acquired with a IXSEA-DELPH system coincidently with most Atacames seismic reflection lines.

3.3. Core Data

Seven 0.88- to 2.44 m-long sediment piston cores recovered in the study area (Figure 1c) using a Kullenberg-type corer were analyzed for lithology, paleoenvironment, biostratigraphy, and ^{14}C dating.

4. Results

4.1. A Tectonic Map of the Cabo-Pasado Continental Shelf

We derive a tectonic map of the shallow-water (<125 m) CP shelf promontory and adjacent Bahia-Jama (BJ) shelf basin, which southwest depocenter (SWBJ) lies in a margin slope re-entrant under 300–600 m of water depth (Figure 1c). The map shows that the axis of the Pliocene-lower Early Pleistocene BJ basin (Hernández et al., 2020) crosses the upper margin slope, extends along the shelf and connects northward to the Pedernales basin (Figure 3). In contrast, the Pleistocene SWBJ depocenters (Hernández et al., 2020) are interrupted over the shelf promontory by a broad composite anticline structure, where deformed Pliocene to lower Early Pleistocene and Middle Pleistocene sediments crop out at the seafloor in water depth locally shallower than 100 m (Figure 3). The map also reveals three main sets of faults and remarkable anticlines: (a) the 45 km-long N40-45°-trending, BJ fault system, i.e., segmented into (i) the South BJ fault (SBJ) that cuts through the SWBJ depocenter, (ii) the Central BJ (CBJ) fault and its associated braided pattern of anastomosing faults (A1–A6) that crosscuts the shelf edge; (iii) the North BJ (NBJ) fault that terminates northeastward across the shelf promontory; (b) the N66°–70°E-trending, 5-18 km-long crustal faults including the Cabuyal fault (Cab) that cuts the inner shelf promontory, and (c) the EW-trending, ∼20 km-long, North and South Canoa faults (SCa and NCa) across the SWBJ depocenter, (d) the N to NE-trending San Vicente anticline which accommodates the transition between the CBJ and NBJ fault segments, (e) the EW-trending CP anticline across the shelf promontory, and (f) the NE-trending Canoa Anticline, which stands astride the upper margin slope and shelf promontory.

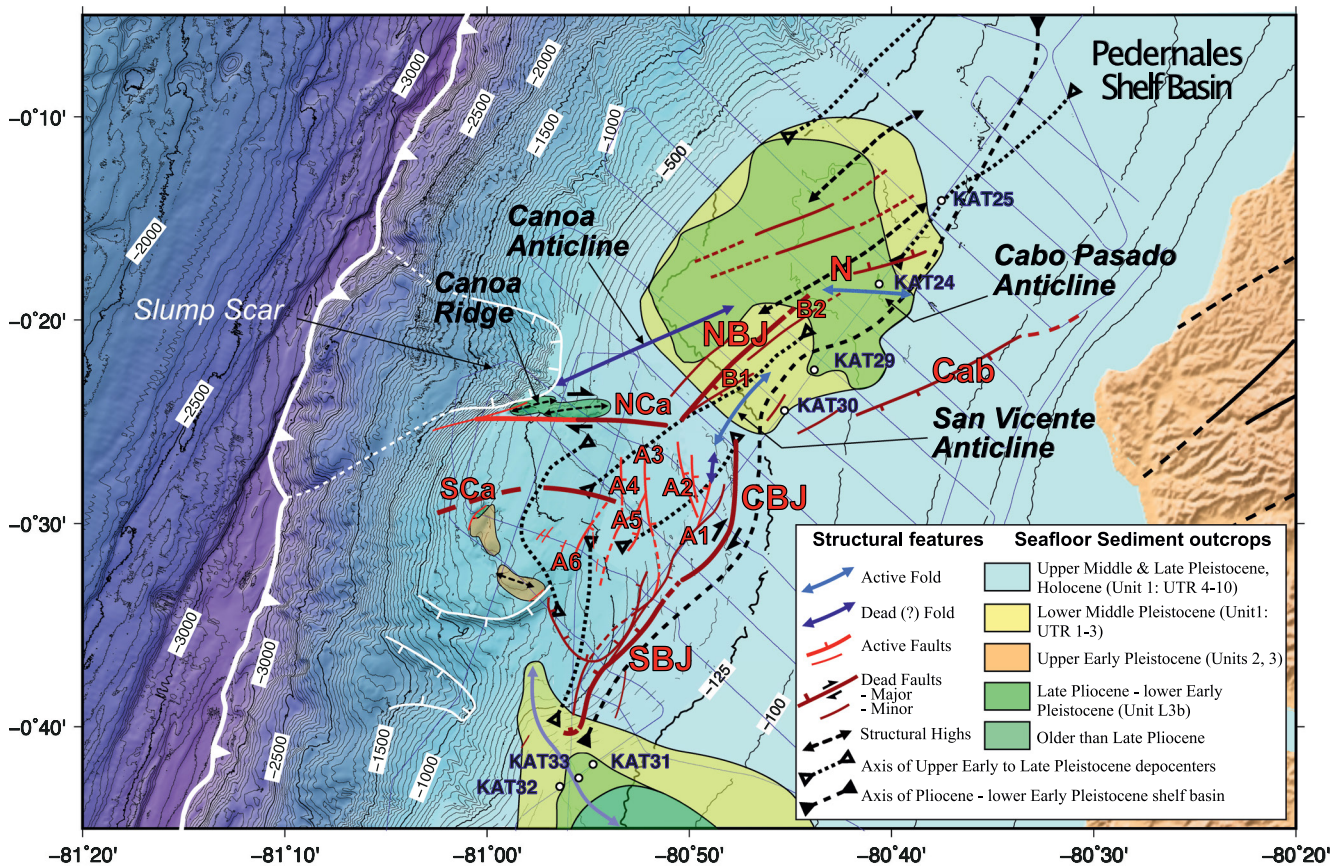

Figure 3. Structural and geological map of the study aera. SBJ, CBJ, and NBJ are South, Central, and North Jama fault segments; Cab is Cabuyal fault; NCa and SCa are North and South Canoa faults. A1–A6 are branching faults; Onshore lineaments = Jama fault system (Reyes & Michaud, 2012); KAT24 to 33 are coring sites; note the broad composite anticline structure associated with the shelf promontory where Late Pliocene-lower Early Pleistocene (light green) and Lower Middle Pleistocene (yellow) sediment outcrop at the seafloor in water depths less than 125 m. Thin blue lines are seismic and chirp data.

4.2. A Crustal Transect Across the Offshore Bahia-Jama Margin Wedge

Deep penetrating line SCAN 900 (Figure 2) cuts across the outer margin wedge from the trench to the shelf edge, and the inner wedge further landward, thus revealing the broad scale structure of the margin wedge and the relationship between the BJ fault system and the plate interface. The plate interface is interpreted at the depth where frontal thrust faults appear to sole out on a more continuous reflective sequence, as well as from intervals of strong reflections between 4 and 6 stwtt (second two-way travel time) (~8 and ~16 km) depths, although they may reflect under-plating making uncertain the actual location of the megathrust. Line SCAN 900 shows the CBJ fault segment to belong to a flower structure (Hernández et al., 2020) that cuts steeply into the margin basement. The fault system projects downward to the megathrust, thus isolating an outer-wedge tectonic sliver from the bulk of the margin. Based on SIS-58 crustal transect (see Figure 4 of Collot et al. (2004)), the East-trending, SCa fault system similarly cuts through the entire margin wedge. Both systems were interpreted as transtensional strike-slip faults whose sustained activity controlled the Pliocene-Pleistocene sediment filling of the 2-3 km-thick BJ basin (Collot et al., 2004; Hernández et al., 2020). The inferred strike-slip mode of the BJ fault system is supported by the 47–52° obliquity between the plate motion direction (N83°E) (Nocquet et al., 2014) and the normal to the fault system (N130-135°E), which, in turn, predicts right-lateral slip (Figure 1c). The quick disappearance of the fault system toward the northeast suggests that only a limited trench-parallel translation of the outer-wedge sliver was achieved, thus representing a very small fraction of the Ecuador large-scale partitioning (Figure 1a) (Nocquet et al., 2014; Pennington, 1981).

4.3. Seismic Stratigraphy of the Pleistocene Sedimentary Cover

Investigating the faults' structural style, and estimating the age of their activity and the vertical motions of the margin wedge are instrumental to identifying temporal changes in the megathrust behavior. This target requires scrutinizing the sedimentary architecture and dating the shelf and upper slope deposits.

Two seismic stratigraphic packages separated by remarkable regional unconformity Uc (noted U5 in Hernández et al. (2020)) are interpreted. The lower package encompasses units L3a and L3b (Figure 2) interpreted as well-stratified, tectonically deformed Pliocene to Lower Pleistocene shelf basin deposits (Hernández et al., 2020). The upper package consists of reflective and well-stratified, 0.05–0.55 stwtt (~37–410 m) -thick, seismic units 1, 2, and 3 that are separated by regional unconformities Ua and Ub (Figures 4–6). Units 1, 2, and 3 are composed of a stack of elementary seismic sequences. In the SWBJ depocenter, 10 elementary sequences were picked up in Unit 1 (UTR 1–10), five in Unit 2 (MTR A–E), and 19 in Unit 3 (LTR F–X) (Figure S1 in Supporting Information S1 and Figure 4). Assuming that climato-eustasy was the main driver of the changes in accommodation space at 100- and ~40-ka time scales during the Pleistocene (Embry, 1993; Proust & Chanier, 2004; Vail et al., 1977), the elementary seismic sequences correspond to Transgression-Regression (T-R) sequences whose bounding unconformities tied to the well-dated transitions between the even and odd marine isotopic stages (MISs) (Lisiecki & Raymo, 2005) provide a time frame for the sediment deposition in the study area (Text S1 and Table S1 in Supporting Information S1).

A biostratigraphic age control based on planktonic and benthic foraminifer assemblages was performed on samples of all piston cores collected in the survey area (Figure 1c). The analysis provides a Late Pliocene to Pleistocene or Holocene age range for most samples (Text S1 and Table S2 in Supporting Information S1; Popescu (2021)). Additionally, sedimentary core KAT25 collected along line 46–1 (Figure 6-i) provided a ^{14}C age of 46,400 cal yr BP and potentially sampled the unconformity between sequences UTR 8 and 9 (Figure S3 in Supporting Information S1). Considering several sources of error presented in Text S1 in Supporting Information S1, the potential ages derived for regional unconformities Ua, Ub, and Uc are 790 ka ± 110, 1031 ka ± 150, and 1832 ka ± 200, respectively. These ages were simplified throughout the text and figures as 0.79, 1.0, and 1.8 Ma. The analysis of the internal sedimentary architecture of the upper package has allowed recognition of Quaternary T-R sequences that are used as a geological time frame to date the tectonic deformation.

4.4. Faulting and Folding Activity

4.4.1. Faulting Activity

The BJ fault system does not have a modern seafloor expression. Instead, in many places, the fault system shows a buried, 75–360 m-high, paleo fault scarp blanketed by 35–150 m of undisturbed sediment (Figures 4 and 7 and Figure S1 in Supporting Information S1) advocating the present-day fault inactivity.

The SBJ fault normally offsets unconformity Uc, indicating that the fault ending postdates Uc. In the SWBJ depocenter, seismic lines ATAC-51 and SCAN-888 (Figure 4 and Figure S1 in Supporting Information S1) show unconformity Uc to have acted as a growth normal fault, a fault that forms contemporaneously with sediment deposition, as supported by the fan pattern of unit 3, the bedding of which laps onto unconformity Uc. The growth fault is interpreted on seismic lines of different orientations (Figure 1c) revealing that extension with a ~NS component occurred near the southern termination of the BJ fault system. In a strike-slip fault environment, this structure can be viewed as a single releasing bend according to the terminology by Mann (2007). The structure, which is bounded at the bottom and top respectively by unconformity Uc and Ub, was mainly active from ~1.8 to ~1 Ma, as was the associated SBJ fault system (Figure 4).

Late shortening affected the growth sequence as indicated by unit 3 internal folding associated with branching fault A1 (Figure 4). Such shortening on a branching fault succeeding to growth faulting argues for a strike-slip component along the SBJ fault. The ultimate shortening terminated with Unconformity Ub, thus pointing the primary ending of the SBJ fault ~1 Ma ago, although residual deformation and auxiliary faults remained active up to unconformity Ua dated ~790 ka (Figures 4 and 8). The ~320/360 m normal offset measured on the SBJ fault scarp in line SCAN 888 (Figure S1 in Supporting Information S1) occurred between unconformity Uc and Ub over ~790 ka providing a mean vertical displacement rate of 0.4–0.45 mm/yr. The growth sequence of Unit 3 is inferred to have recorded T-R sequences, as well as the integrated fault slip that resulted from co-seismic

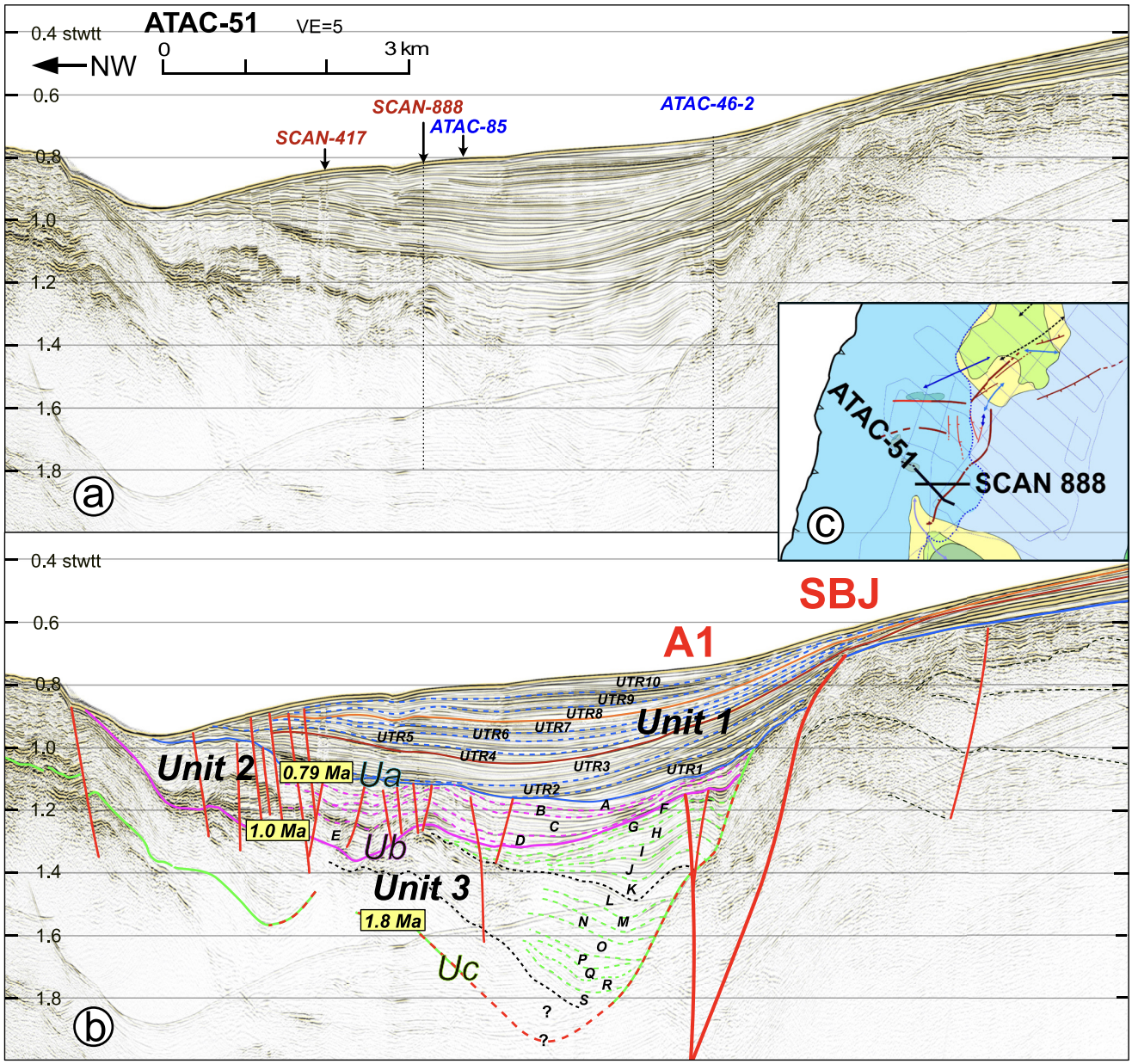

Figure 4. Seismic reflection line ATAC-51 across the SW Bahia-Jama depocenter and A1-SBJ fault system (vertical red lines). (a) Un-interpreted section with crossing seismic lines. Depth in stwtt (second two-travel time); VE= Vertical exaggeration; (b) interpreted section indicates Units 1, 2 and 3, major unconformities Ua, Ub, and Uc and the fan shape structure of Unit 3. Dashed red line indicates that unconformity Uc was a growth normal fault (see text and Figure S1 in Supporting Information S1). Names and lettering UTR 1–10, A–E, and F–S within the units refer to elementary seismic sequences interpreted on line SCAN-888 (Figure S1 in Supporting Information S1); thin red and orange lines are respective base of regionally interpreted elementary seismic sequences UTR4 and UTR8. Ages of major unconformities are determined on the basis of the sequential stratigraphy and piston core data (Text S1 and Table S1 in Supporting Information S1). (c) Map showing line location.

increments of the fault growth and the SBJ fault scarp development, although both controls on sedimentation cannot be disentangled.

The CBJ fault is part of the flower structure identified in crustal section SCAN 900 (Figure 2). CBJ is associated with a remarkable pattern of stratal deformation in which, L3b reflectors from both sides of the fault dip asymmetrically toward the fault where they are truncated (Figure 7) and Hernández et al. (2020). Although fan patterns associated with branching faults A2 and A3 in line SCAN 900 (Figure 2) show evidence of extension during L3b deposition (Hernández et al., 2020), the bulging of the units L3a and L3b jammed between CBJ and A2 faults

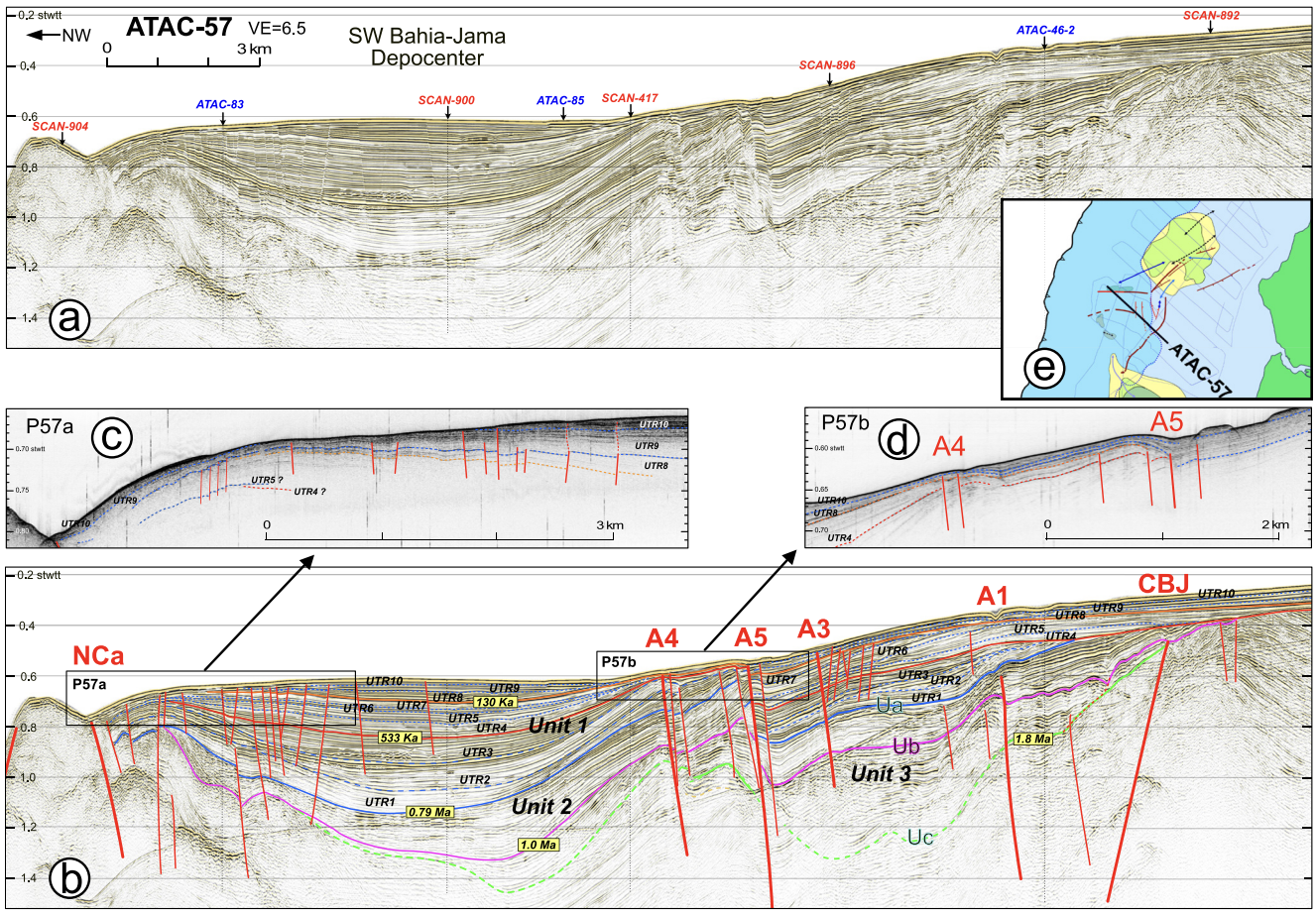

Figure 5. Seismic reflection line ATAC-57 and Chirp data across the SW Bahia-Jama depocenter, the western segment of the North Canoa (NCa) fault, and the A4 -A5 and Central Bahia-Jama fault segment (CBJ); (a) un-interpreted section with crossing seismic lines; (b) interpreted section (see Figure 4 for caption); (c) and (d) Chirp data showing latest sequences of Unit 1 (UTR 8-9-10) to be deformed respectively by the NCa fault (c), and A4 and A5 faults (d) (see text); (e) map showing line location.

argues for a late shortening phase. Altogether, these observations confirm strike-slip along the CBJ fault. The CBJ fault scarp primarily resulted from repeating ruptures that preceded the scarp erosion by unconformity Uc (Figures 2, 6 and 7). The bedding of unit 3 laps onto the CBJ fault scarp, supporting that the fault activity had ceased by Uc, ~1.8 Ma ago (Figure 8).

Branching faults A2–A6 are short in map view and distribute extensional deformation across the fault network (Figure 3). According to Chirp data (Figure 5d), faults A4 and A5 deform the seafloor and the ~14-ka-old UTR 10 sequence, suggesting a recent activity (Figure 8).

The NBJ fault vanishes near the CP Anticline (Figure 3). The NBJ fault is blind on seismic lines ATAC-59, 61, and 62 (Figures 7, 9 and 10) and buried beneath ~300 m of unit 1 sediment on line ATAC-59 (Figure 7), whereas branching faults B1 and B2 crop out at the seafloor in lines ATAC-61 and 62 (Figures 9 and 10). Comparing the structural configuration of post-Uc units on lines ATAC-59 and 61 helps date the recent outer shelf deformation and the ending of the NBJ fault activity. Both lines reveal a remarkable marker of the deformation, which is a poorly reflective layer interpreted as a ~75 m-thick mass transport deposit (MTD) based on its poor reflectivity and strata truncated along its basal surface in line ATAC-59 (Figure 7). On line ATAC-59, the MTD accumulated in a syncline flanked by the Canoa and San Vicente anticlines, implying that shortening predated the MTD. The wavy shape of its section further argues for the post-MTD continuation of the shortening. On line ATAC-61, the syncline was inverted into an anticline, denoting the northward propagation of the San Vicente anticline, leading to the truncation of UTR1 strata at the seafloor (Figure 9c). On line ATAC-61, UTR1 strata thicken substantially seaward implying that a depocenter developed farther trenchward during a short subsidence between 790

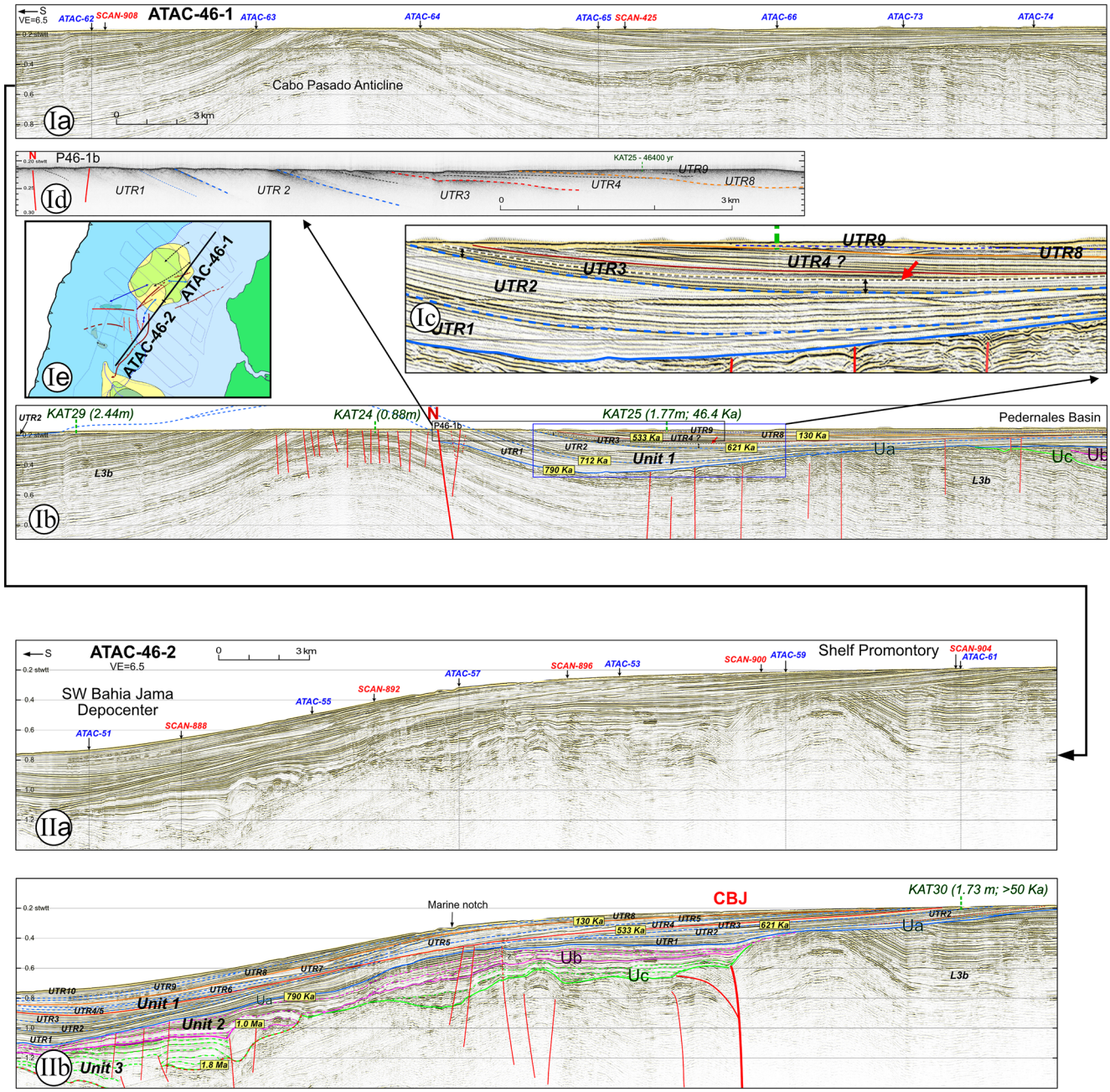

Figure 6. Seismic reflection line ATAC-46-1 and its continuation 46-2 from the Pedernales basin through the Cabo Pasado anticline and the shelf promontory to the SW Bahia-Jama depocenter; Top (Ia) un-interpreted section with crossing seismic lines across the Cabo Pasado (CP) Anticline and Fault N; (Ib) interpreted section shows structures and inferred ages. Unconformities Ub and Uc are interpreted near the northern end of the line, whereas, Units 1 and L3b outcrop at the seafloor respectively North and South of fault N; see Figure 4 for stratigraphy and ages caption. KAT 24, 25, and 29 are sedimentary cores with their length. (Ic) Zoom imaging the northward diverging pattern of lower strata of sequence UTR3 (black double arrows beneath the red arrow) that opposes the southward diverging pattern of sequences UTR1 and 2, thus dating resumption of the anticline growth; (Id) Chirp data shows that unit 1 sequences up to UTR 8 and 9, are tilted and truncated at the seafloor defining a sediment-bare morphology with subtle irregularities; (Ie) map showing the location of the two segments of line 46; Bottom (IIa) un-interpreted section of line 46-2 with crossing seismic lines showing the geological structure across the Central Bahia-Jama faut system (CBJ); (IIb) interpreted section (see Figure 4 for Stratigraphy and ages caption). Note that Units 2 and 3 are found only south of the CBJ fault implying a ~1 Ma-long hiatus on the shelf promontory (see Figure 8). KAT30 is sedimentary core dated older than 50 ka.

and 712 ka. Instead of thickening seaward, the lower strata of overlying sequence UTR2 (Figure 9c) thickens landward so that the age of this reversal allows dating the propagation of the San Vicente anticline and, on the whole, the resumption of the outer-shelf shortening and uplift, to lower UTR 2 deposits, likely between 712 and

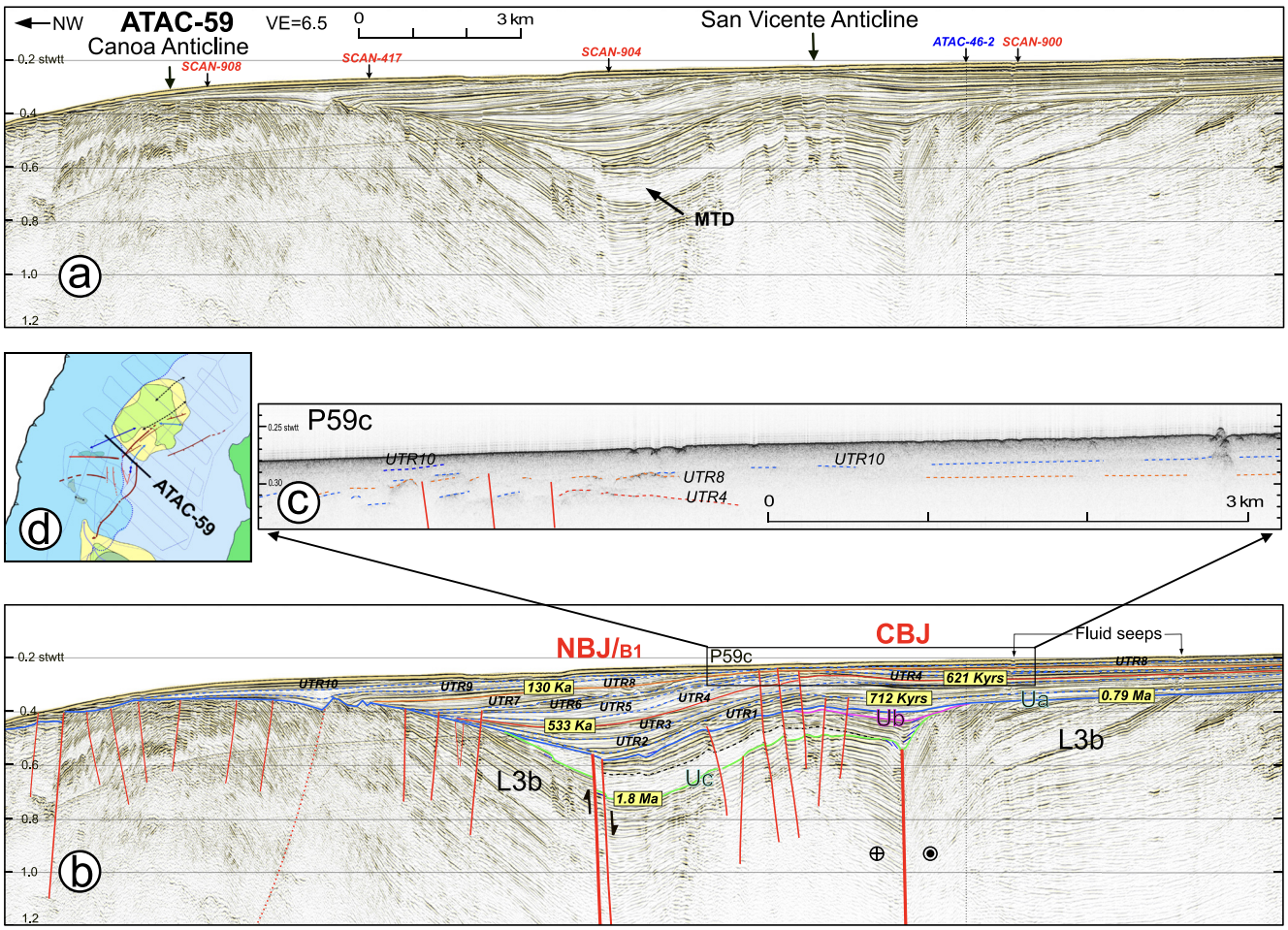

Figure 7. Seismic reflection line ATAC-59 and Chirp data imaging both the North Bahia Jama (NBJ)/B1 fault and the Central Bahia-Jama fault segments (CBJ), as well as the Canoa and San Vicente anticlines. (a) Un-interpreted section with crossing seismic lines; MTD = Mass Transport Deposit; (b) interpreted section (see Figure 4 for stratigraphy and ages caption). Unconformity Uc (light green) sealed the CBJ strike-slip fault and its paleo scarp, whereas NBJ/B1 faults were sealed near unconformity Ua (blue). Note the MTD laid in a syncline prior to be offset by NBJ fault and deformed by the growing San Vicente anticline; (c) Chirp data suggests that the shallow sequences of Unit 1 (UTR 4 and 8) are faulted above the San Vicente anticline; (d) map showing line location.

676 ka (Table S1 in Supporting Information S1). The timing of subsidence and subsequent uplift are further confirmed farther north in line ATAC-65, where both a seaward thickening of UTR1 strata and a reversal of stratigraphic divergence during the deposition of UTR2 lower strata are also documented (Figure S4c in Supporting Information S1).

The end of the NBJ Fault and fault B1 activities can as well be estimated from seismic lines ATAC-59 and 61 (Figures 7 and 9), where the faults normally offset the MTD by ~50–55 m. The upthrown section of the MTD was truncated by unconformity Ua, which, on line ATAC-59, is slightly offset by fault NBJ. The fault was sealed by UTR1 early deposits implying that the fault ended during the ~790–712 ka time interval. In line ATAC-61 (Figure 9c), the upthrown section of the MTD is truncated by Unconformity Ua, which, in turn, was shifted vertically by a few meters across fault B1. The fault tip is associated with a 3-m-high seafloor bump (Figure 9d) that could result either from a recent fault reactivation or from differential erosion. Several seabed irregularities associated with un-faulted, tilted beds elsewhere along line ATAC- 61 (Figure 9d) appear to result from erosion of beds of variable hardness, suggesting a similar origin for the bump associated with fault B1, which is thus considered inactive, as already evidenced on line ATAC-59 (Figure 7). Therefore, the NBJ fault system likely ceased activity ~790–712 ka ago, during the subsidence period and shortly before a new shortening and uplift phase began affecting the shelf promontory 712–676 ka ago (Figure 8).

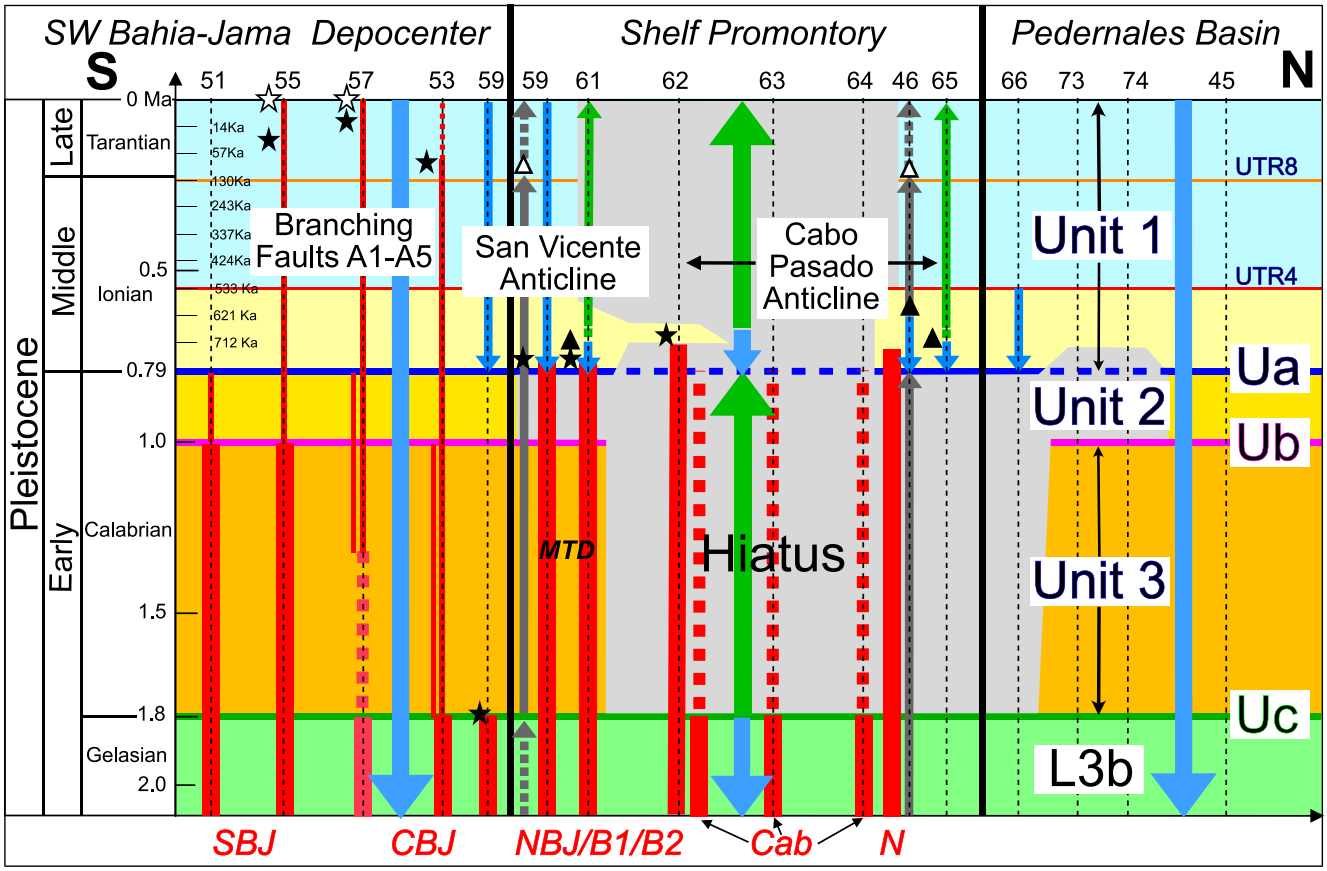

Figure 8. Chronostratigraphic correlation of Pleistocene units 1, 2, 3, and L3b deposits, and unconformities Ua, Ub, and Uc along a strike section across the Cabo Pasado (CP) shelf promontory based on interpretations of NW-trending ATAC seismic lines (line numbers at top) and strike line ATAC 46 (Figure 6); units color as in Figure 3; thick red bars: major fault activity (SBJ, CBJ, NBJ = South, Central and North Bahia-Jama fault segments, and faults B1, B2, fault N and Cab (projected Cabuyal Fault); thin red bars: A1–A5 branching faults activity; stars: last evidence of faulting activity from seismic or chirp data (black), from seafloor morphology (white); triangles: first (black) and last (white) evidence of uplift/fold growth; pale blue arrows = subsidence; green arrows = uplift; gray arrows: growth of San Vicente and CP anticlines.

The Cabuyal Fault (Cab) is blind and normally offsets unit L3b by ~50 m (Figure 10). The fault-created topography in unit L3b was eroded by unconformity Ua. However, the regional stratigraphic correlation indicates that unconformity Ua is locally overlain by ~40 m of UTR2 deposits dated ~712 ka (Figure 10), suggesting that the Cab fault activity could have stopped at any time during the ~1 Ma-long hiatus defined between unconformity Uc, which truncated unit L3b ~1.8 Ma ago, and the oldest UTR2 deposits (Figure 8). Due to its location and trend, the Cab fault is likely to be associated with the offshore projection of a strand of the onshore Jama fault system (Figure 3) (Reyes & Michaud, 2012).

The NCa and SCa faults bound an EW-elongated and buried paleo-basement high topped by a strong reflector (Figures 2 and 11). The reflector is remarkably smooth and contrasts with its elsewhere jagged appearance indicating that the basement high was heavily eroded. The erosion occurred during the probable emergence of the basement high at the Miocene-Pliocene boundary (~5 Ma) as inferred from its L3a sedimentary cover tentatively dated Pliocene by Hernández et al. (2020). The Canoa faults, which have controlled the vertical motions of the basement high, share a similar EW trend with a set of Oligocene to early middle Miocene normal faults imaged offshore CP by Hernández et al. (2020), indicating that they might be co-genetic. The NCa and SCa faults show, however evidence for strike-slip motion. The SCa fault is correlated with a deep-seated flower structure (see Figure 4 of Collot et al. (2004), which shows poor evidence of activity since unconformity Ua, that is, ~790 ka (Figure 11). The NCa fault is associated in map view with the small Canoa ridge, where deformed Paleogene to Miocene rocks (Figure 3) crop out at the seafloor (Hernández et al., 2020). The ridge consists of two en-échelon segments that trend ENE, oblique to the fault trend (Figure 3) implying a dextral component of

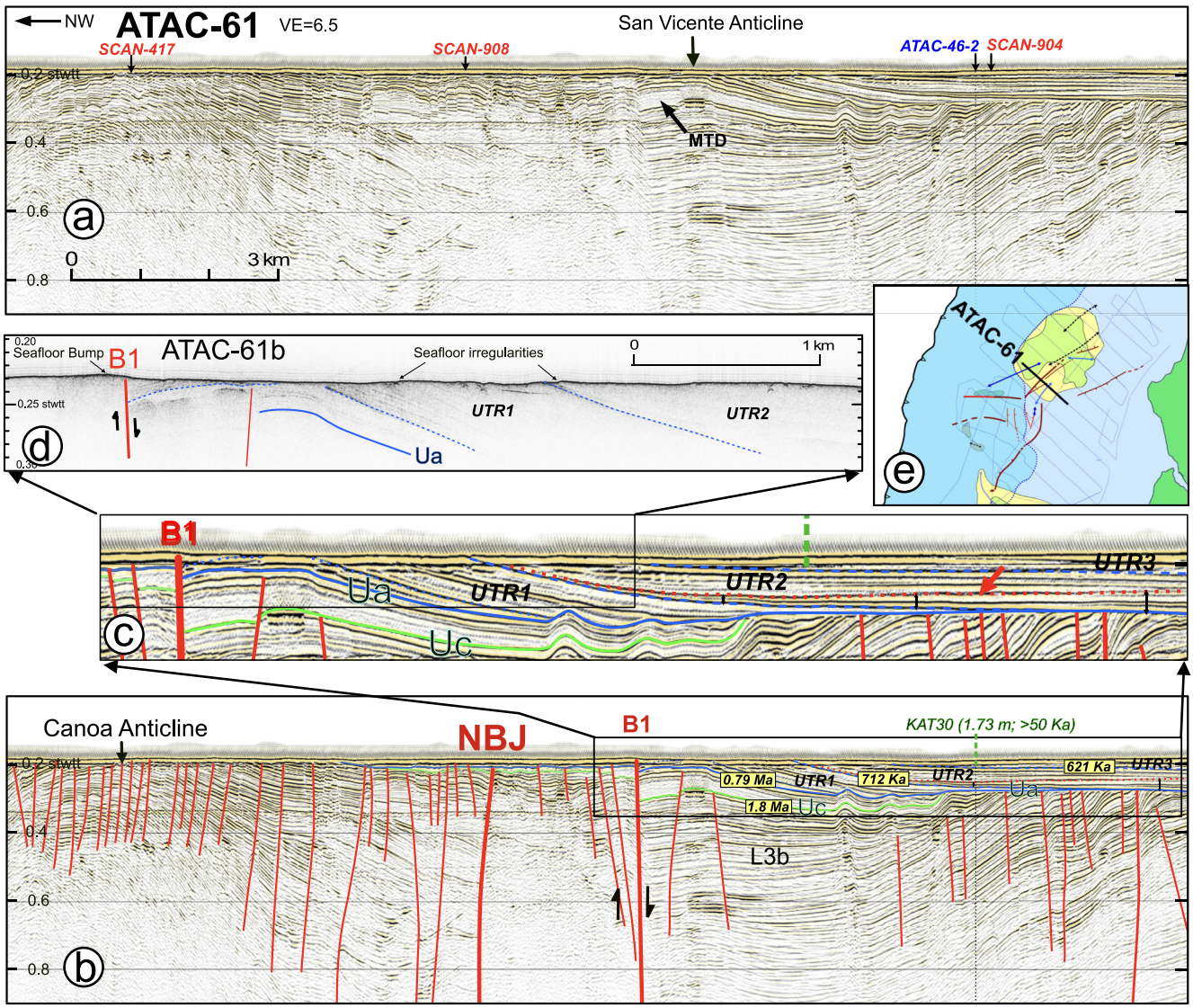

Figure 9. Seismic reflection line ATAC-61 and Chirp data across the North Bahia Jama (NBJ)/B1 faults, and Canoa and San Vicente anticlines. (a) Un-interpreted section with crossing seismic lines; MTD (Mass Transport Deposit); (b) interpreted section (see Figure 4 for stratigraphy and ages caption). Note that the MTD identified in line ATAC-59 (Figure 7), was inverted with the San Vicente anticline, and offset vertically by fault B1; (c) zoom imaging the landward diverging pattern of lower strata of sequence UTR2 (thin black double arrows beneath the red arrow) that opposes the trenchward diverging pattern of sequence UTR1 thus dating the recent uplift of the outer shelf (see text); (d) Chirp data showing the faulted apex of the San Vicente anticline and subtle (~3 m) seafloor bump associated with fault B1 and landward tilted UTR beds; (e) map showing line location.

strike-slip deformation. Line SCAN 417 (Figure 11) does not show evidence for post-790 ka NCa fault reactivation. However, further west along the NCa fault, sediments of Unit 1 are faulted and bulge upward over the buried part of the ridge (Figure 5) indicating that tectonic deformation occurred since unconformity Ua ~790 ka. Chirp data (Figure 5c) show sequences UTR8 and 9 to be faulted and folded suggesting that the NCa fault activity continued until ~57 ka, and possibly up to 14 ka as indicated by UTR10 faint, diverging reflectors evoking sedimentary progradation at the toe of the slope (Figure 5c).

4.4.2. Folding Activity

The San Vicente anticline initiated during the late shortening that deformed the lower package (units L3a and b) of sediment between A2 and CBJ faults in line SCAN-900 (Figure 2). This shortening generated a transpression push-up, which locally inverted the BJ basin. Although folding appears to have ended by unconformity Uc on line SCAN-900, synchronously with the stopping of CBJ fault, the growth of the San Vicente anticline continued

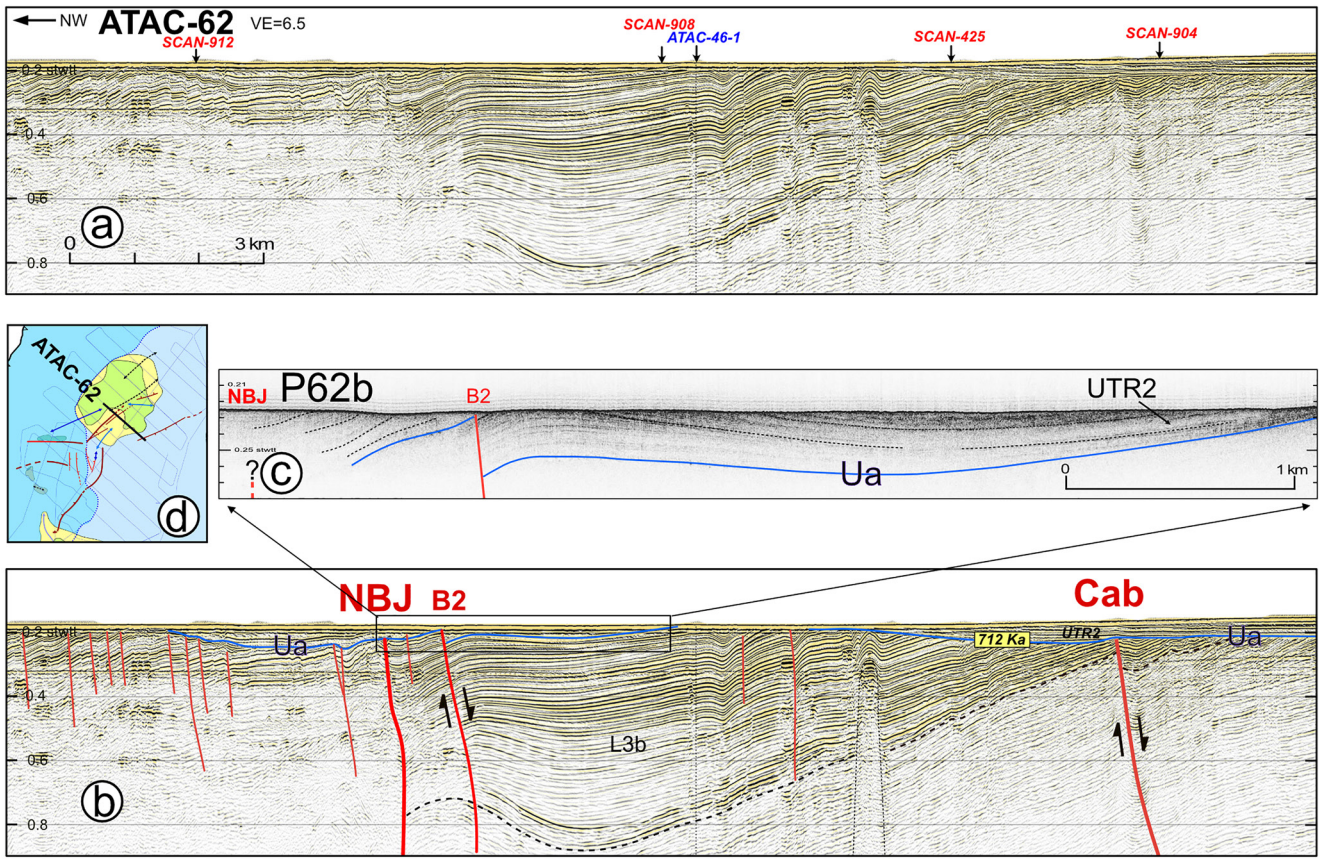

Figure 10. Seismic reflection line ATAC-62 and Chirp data across the North Bahia Jama (NBJ)/B2 and Cabuyal (Cab) faults. (a) Un-interpreted section with crossing seismic lines; (b) interpreted section (see Figure 4 for stratigraphy and ages caption). Note that fault B2 offsets vertically unconformity Ua (blue) and that sequence UTR2 sealed the Cabuyal fault which offsets unit L3b; (d) Chirp data shows fault B2 and associated deformed strata; (d) map showing line location.

immediately north, after unconformity Uc, as exemplified on lines ATAC-59 and 61 (Figures 7 and 9). Indeed, the stratigraphic analysis of line ATAC-59 (Figure 7) indicates that the anticline grew at least up to ~130 ka (UTR8) as substantiated by: (a) the upward bulging of UTR sequences over the anticline, (b) the progressive seaward migration of their depocenters, and (c) the disruption by normal faults within the anticline of regional unconformities as young as the base of T-R sequences UTR4 (533 ka) and UTR8 (130 ka) interpreted as former hard grounds (Figures 7c and 8).

The CP Anticline developed immediately north of the ending of the BJF system (Figure 3). The analysis of Line ATAC-46-1 (Figure 6) allows documenting the anticline's growth and the shelf promontory's vertical motions. The southward-diverging pattern of UTR1 and UTR 2 strata indicates that a small depocenter and correlative subsidence had developed in the region of the CP Anticline over the 790–621 ka time period. Normal fault N that offsets the anticline by ~ 45 m (Figure 6) was sealed during UTR1 deposits as indicated by a neighboring SCAN profile (Figure 5b in Hernández et al. (2020)) suggesting that the fault activity stopped during the subsidence period. Unit 1 sequences also recorded a recent phase of the anticlinal growth. The unconformity at the base of sequence UTR3 separates the southward-diverging strata of UTR1 and UTR 2 sequences from overlying, northward-diverging strata of UTR3 (Figure 6c), allowing to dating the shortening phase initiation to the early deposits of UTR3, that is, to ~621–563 ka. The base of sequences UTR4 and UTR8 potentially identified on Chirp data (Figure 6-Id) is tilted northward and truncated at the seafloor, implying that the anticline growth continued at least until ~130 ka (Figure 8).

The Canoa Anticline (Figures 7 and 9) severely deforms units L3b and older units, seaward of the NBJ fault. Line ATAC-59 (Figure 7) shows that unconformity Uc was jointly deformed with the L3b strata involved in the anticline, prior to being truncated by unconformity Ua, suggesting that folding climaxed sometimes during the ~1-Ma-long sedimentary hiatus tentatively dated between ~1.8 and 0.79 Ma over the anticline. Additionally,

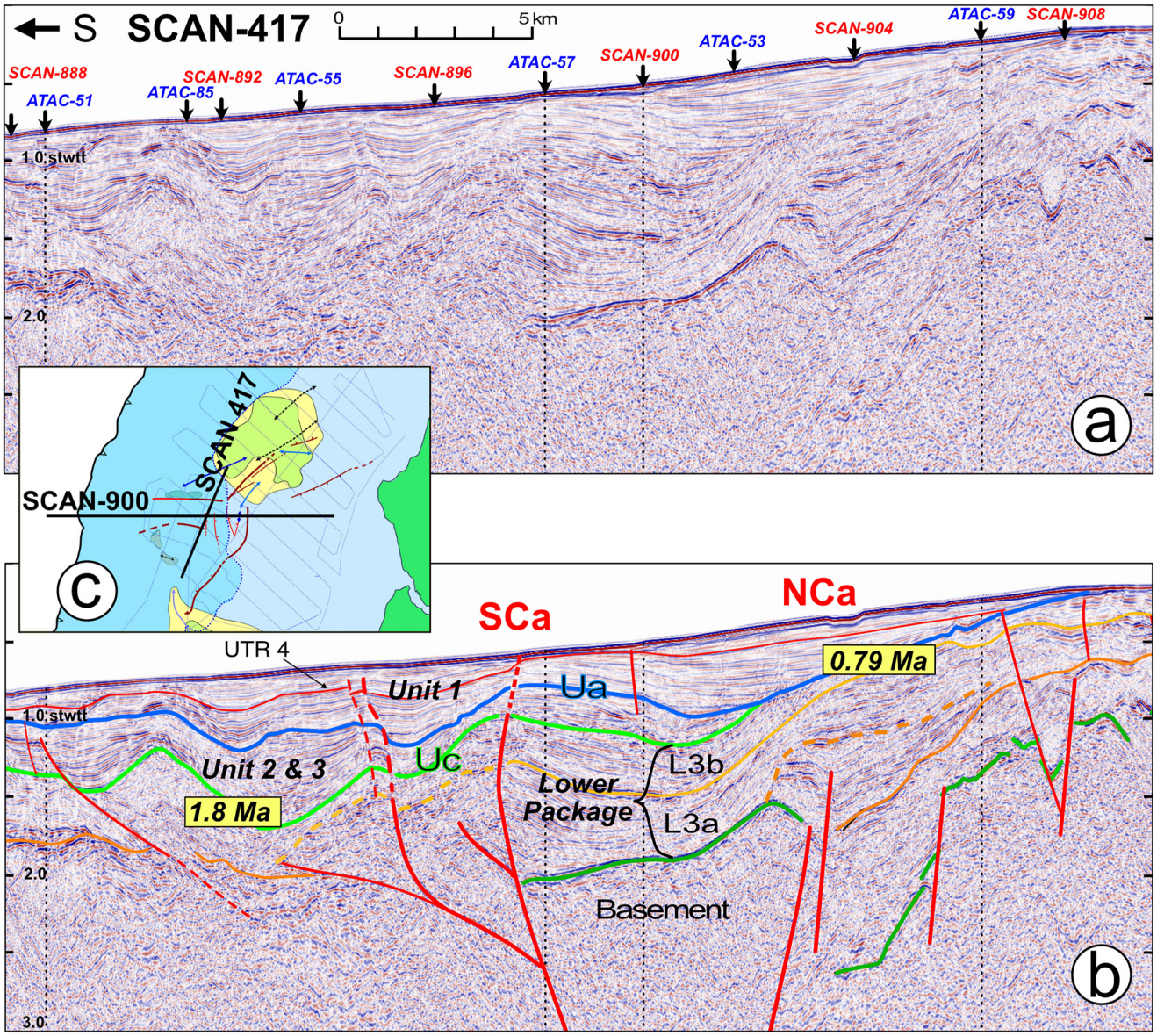

Figure 11. Seismic reflection line SCAN-417 across the North (NCa) and South (SCa) Canoa Faults; (a) un-interpreted section with crossing seismic lines; (b) interpreted section (see Figures 2 and 4 for stratigraphy caption). Note the strong reflector (dark green) returned by the eroded top of the basement high also identified in crossing line SCAN 900 (Figure 2). This segment of NCa fault is blind and sealed, whereas that of SCa fault might still accommodate deformation; (c) map showing line location.

most normal faults that have developed across the hinge of the anticline do not offset unconformity Ua, and this erosional surface is gently overlain by undeformed sequences of unit1, arguing that the fold is no longer active (Figure 7).

5. Discussion

The results presented above reveal the timing of specific steps of the cumulative deformation of the margin wedge offshore CP. In the discussion, we explore the more suitable conditions of the long-term plate coupling that best account for specific steps of the deformation and lead to the CP and J geodetically locked patches.

5.1. An Outer-Wedge, Long-Term Inter-Plate Coupling Prior to ~1.8 Ma

In oblique convergence settings, strike-slip faulting is a response to strain partitioning when the megathrust accommodates trench-normal slip, and a trench-parallel margin fault takes up the lateral component of slip (Fitch, 1972). This process leads to the formation of a forearc sliver that moves along the margin (Jarrard, 1986b) as long as it is not opposed by a buttress related to geometrical or inter-plate frictional conditions (Beck et al., 1993). Strike-slip faulting often occurs along the volcanic arc because thermal softening makes it the weakest part of the overriding plate (Beck, 1983). Trench-subparallel, strike-slip faulting is further documented closer to the trench, in accretionary wedges for example, along the Puerto-Rico (ten Brink & Lin, 2004), and southern Ryukyu trenches (Lallemand et al., 1999), and in fore-arc basins for example, along the Mentawai fault zone offshore Sumatra (Berglar et al., 2008; Diament et al., 1992). In addition to the convergence obliquity, which is a necessary condition met in our study zone, the dominant factors controlling strain partitioning stand as the plate coupling, and a low strength zone or mechanical heterogeneity in the margin wedge (Chemenda et al., 2000; Jarrard, 1986b; McCaffrey, 1992; McCaffrey et al., 2000). Indeed, the outer-wedge, long-term plate coupling must exceed the strength of the strike-slip fault to drag the fore-arc sliver effectively along the trench.

Offshore central Ecuador, wide-angle seismic data (Graindorge et al., 2004) and local earthquake tomography (León-Ríos et al., 2021) suggest that the nature of the margin's basement is consistent with oceanic terranes similar in petrology to the late Cretaceous to Paleocene basement rock that outcrops onshore (Baldock, 1983; Jaillard et al., 2009; Luzieux et al., 2006). The BJ and Canoa fault systems are believed to cut through the entire oceanic basement (Figure 2 and Collot et al. (2004)). They trend respectively ~NE and E-W, sub-parallel to regional faults (Reyes & Michaud, 2012) known onshore to be ancient faults that bound or cut through accreted oceanic blocks (Luzieux et al., 2006), thus pointing to mechanically weak, inherited faults prone to be re-mobilized in a well-oriented stress field (Agurto-Detzel et al., 2019). The consideration that the convergence obliquity remained high over the last millions of years (Somoza & Ghidella, 2012), and that the BJ strike-slip fault was active allows inferring that the shallow megathrust was coupled beneath the outer-wedge tectonic sliver.

The 75–360-m-high paleo-scarp and the growth faulting associated with the activity of the SBJ and CBJ Fault segments prior to about 1 Myr are considered evidence for large earthquakes to have produced repeated paleo-seafloor ruptures along the fault system such as interpreted for Holocene splay fault seafloor scarps in Southern Prince William Sound, Alaska (Liberty et al., 2019). Such inferred BJ fault paleo-seafloor ruptures also support local plate coupling.

The inception of the BJ fault system can be documented as well. As observed in worldwide examples of large-scale buttressed fore-arc slivers controlled by a margin parallel strike-slip fault (Jarrard, 1986a; Wang, 1996), the CP anticline denotes trench-parallel compression at the leading edge of the buttressed outer-wedge sliver, thus potentially relating the anticline formation to the BJ fault system activity. Accordingly, the initiation of the anticline during the late early Pliocene tectonic inversion of a local depocenter (Hernández et al., 2020) provides a clue for the timing of reactivation of the BJ fault system, and therefore the onset of a relative, outer wedge plate coupling.

Plate coupling at the shallowest portion of the megathrust has been shown to be consistent with seafloor geodetic observations offshore Peru (Gagnon, 2005), and Nankai (Yokota et al., 2016) and with substantial shallow co-seismic slip during the Tohoku-Oki earthquake (Loveless & Meade, 2011). Because the absence of off-shore geodetic data limits the ability to resolve outer wedge inter-plate coupling, GPS data collected onshore Central Ecuador allow a wide range of GPS models that consider either no or a medium inter-seismic coupling west of the SBJ fault system (Chlieh et al., 2014; Gombert et al., 2018; Rolandone et al., 2018). However, the past activity of the BJ fault system suggests that although non-quantified, long-term, inter-plate coupling was permitted beneath the outer wedge sliver prior to ~1.8 Ma.

5.2. The Cabo-Pasado and Jama Locked Patches: Results of a Local Increased Plate Coupling Since ~1.8 Ma

The abandonment of the BJ fault system was progressive as attested by the ~1.8–1 Ma, limited ~NS extension documented in the releasing bend, and the inferred latest deformation along branching fault A1 (Figure 4). This abandonment could have resulted from an overall reduction of the outer wedge inter-plate coupling, which became inefficient enough to prevent slip partitioning. Alternatively, a relative increase of the inter-plate coupling focused

beneath the shelf promontory would have slowed down or even inhibited the translation of the outer-wedge sliver as suggested by structural evidence in other regions (Beck, 1983).

According to physical and numerical models based on the Coulomb wedge theory (Dominguez et al., 2000; Lallemand et al., 1994; Ruh et al., 2013), depending on the strength and geometry of the wedge, subduction along a planar and weak megathrust produces less off-fault margin deformation and topography than along a rough and strong plate interface where the subduction deforms the margin wedge severely by shortening and uplift in the convergence direction. In the region of the CP shelf promontory, the post- ∼1.8 Ma tectonic history supports the hypothesis of a relative increase in plate coupling. Indeed, the phase of shortening, which succeeded the Pliocene -lower Early Pleistocene period of fore-arc basin subsidence recorded by unit L3 deposits (Hernández et al., 2020), terminated by the uplift and vigorous erosion of deformed unit L3b (Figure 6). This phase peaked during the ∼1.8–0.79 Ma sedimentary hiatus outlined by unconformity Ua on the shelf promontory (Figure 8). Additionally, the shallowness of unconformity Ua suggests that the shelf promontory emerged during early Pleistocene sea-level lowstands (Hansen et al., 2013). Subsequently to its emergence and severe erosion, the whole shelf promontory subsided over the 790–712 ka time gap before uplift and landward tilt resumed during the 712–621 ka time interval, as interpreted from UTR1 and 2 internal architectures at both extremities of the shelf promontory (Figure 9 and Figure S3 in Supporting Information S1). Uplift of the whole shelf promontory proceeded after 621 ka as indicated by the southward progradation of sequences younger than UTR2 (Figure 6), as well as by the northward (Figure 6) and landward (Figure S4 in Supporting Information S1) migration of the depocenters of these sequences. The deformation amplified locally with the resumption of the growth of the CP anticline over the 621–533 ka time gap as interpreted from UTR3 internal deposits (Figure 6c). Overall, this new phase of deformation caused unconformity Ua and younger strata of the shelf promontory to be truncated at the seafloor during high-amplitude (∼120 m), Middle to Upper Pleistocene low sea level stands (Hansen et al., 2013; Miller et al., 2005), while over areas of the inner shelf, sedimentation proceeded since UTR3, in the form of condensed sequences. In our data set, disrupted hard grounds and tilted beds as young as 130 ka (UTR8), 57 ka (UTR9), and possibly 14 ka (UTR10) are the most recent traces of the ongoing tectonic deformation associated with the San Vicente (Figure 7c) and CP anticlines (Figure 6-Id).

In conclusion, the shortening and uplift history of the shelf promontory, which had initiated in the mid-early Pleistocene (∼1.8 Ma) after a long period of subsidence, points to a major change in the stress regime beneath the shelf promontory. The enduring shortening indicates that the margin wedge has long been in a compressively critical state implying a long-term plate coupling. The spatial correlation between the CP locked patch and the uplifted shelf promontory, which has been deforming for a hundred thousand years (Figure 12) indicates the persistence of the long-term plate coupling until the present. The Cabo-Pasado and Jama locked patches are therefore considered as present-day representatives of the long-term plate coupling. This coupling could originate either from long-lived, high-basal friction (Wang, 2010; Wang & Hu, 2006), or a geometrical resistance to the fault motion due to a rugged subducting seafloor (Wang & Bilek, 2014). Finally, our result points to long-term operating tectonic mechanisms linking the megathrust mechanical behavior and the buildup of permanent fore-arc deformation offshore central Ecuador.

5.3. Subduction of the Carnegie Ridge Crest

5.3.1. A Cause for the Long- and Short-Term Plate Coupling in the Cabo Pasado Area

Subducting rough topography is believed to exert a strong control on the structural development of convergent margins (Dominguez et al., 2000; Ruh et al., 2016), although its role in inter-plate coupling and seismogenesis is still disputed (Bassett & Watts, 2015; Collot et al., 2017; van Rijsingen et al., 2018; Wang & Bilek, 2014). In Ecuador, the relationship between subducted CR and the fore-arc structure has long been pointed out (Collot et al., 2004; Gutscher et al., 1999; Lonsdale, 1978). Due west of the study area, the crest of the eastern CR consists of a ∼40–60-km wide, volcanic basement swell with peaks barren of sediment, which culminates at a ∼650 m-water depth (Lonsdale, 1978). Although the seafloor morphology prior to subduction may not fully reflect the inter-plate morphology, the residual bathymetry of the Ecuador margin, which was obtained by subtracting an averaged topography from the bathymetric grid, is highest over the outer wedge in our study zone and is interpreted to be due to the subducted eastern CR (Agurto-Detzel et al. (2019).

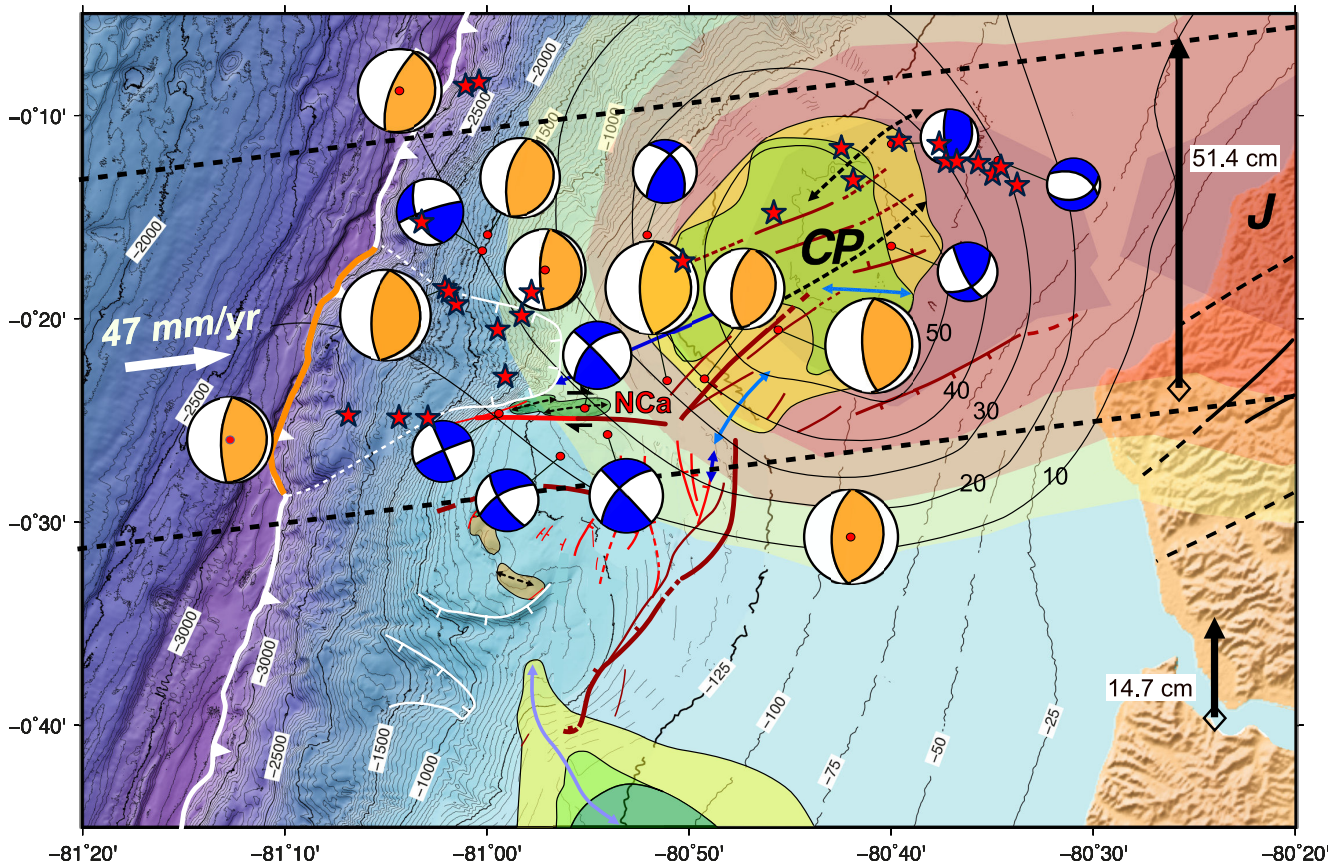

Figure 12. Structural map showing focal mechanisms of the 2016 aftershock sequence and other geological and geophysical information within a N-83°E trending corridor bounded by the two parallel dashed lines. The corridor includes (1) the shallowest Ecuadorian trench segment (orange segment of the deformation front), (2) a morphologic scar in the outer wedge, (3) the shallow shelf promontory and its broad composite green and yellow anticline structures (see geology caption in Figure 3), (4) the Cabo-Pasado and Jama locked asperities (CP and J dark orange-yellow pattern, see Figure 1c); (5) the 30-day after slip of the Mw 7.8, 2016 earthquake (thin black contours every 10 cm after Rolandone et al., 2018); (6) repeating earthquakes (red stars) identified over a ∼1 year period after the 2016 earthquake (Chalumeau et al., 2021); and (7) the highest (51.4 cm) 2016-co-seismic uplift (vertical black arrow) (Nocquet et al., 2017). The alignment of the northern cluster of repeaters departs from the fault trends and may outlines structures of the north flank of the subducting CR crest, while the near-trench cluster concentrates beneath the outer wedge scar left in the wake of the subducting CR crest. Orange beach balls are thrust focal mechanisms from gCMT catalog (https://www.globalcmt.org); blue ones are from Leon Rios et al. (2019). Note that four 2016 strike-slip focal mechanisms are associated with the Canoa fault system (NCa).

In more detail, we consider that the conspicuous alignment along a N83°E-trending corridor parallel to the plate convergence direction (Figure 12) of (a) the shallowest Ecuadorian trench segment, (b) a remarkable slump scar left in the outer wedge (Figure 3), (c) the shallowest and highly deformed shelf promontory, (d) the Cabo-Pasado and Jama locked patches, (e) the highest 2016-co-seismic uplift (∼51.4 cm) and greatest seismic moment released (Figure 1b) in the Jama-CP onshore area (Nocquet et al., 2017), and (f) the coastal exposure, west of Jama city (Figure 1b), of Upper Early Pleistocene inner-shelf to fluviatile deformed sediment (Cantalamessa et al., 2005) supports the hypothesis that the Cabo-Pasado and Jama locked patches correlate with CP and J subducted reliefs of the CR crest. With respect to the 30 km NS extent of the uplifted shelf promontory, a reasonable size for the footing of the reliefs would range from 40 to 50 km. The subducted reliefs hypothesis seems reasonable as the CP shelf promontory shares similar characteristics of inter-seismic coupling level and depth, slow-slip mode (Rolandone et al., 2018), bathymetry and tectonic history with the La Plata area (Proust et al., 2016) (Figure 1a), the locked patch of which is caused by a subducted oceanic relief of the CR (Collot et al., 2017). According to this hypothesis, the CP and J locked patches would rather be caused by an irregular geometry of the plate inter-face than only by patches of high-basal friction. Indeed, the CP-locked segment of the megathrust is considered relatively weak as it slipped aseismically after the 2016 event and was the site of three slow-slip events (SSEs) since 2010 (Rolandone et al., 2018). The geometrical resistance interpretation suggests that the locked patches did not remain stationary but instead moved along with the subducted reliefs.

5.3.2. A Subduction Scenario for the CR Crest

To further test the subducted reliefs hypothesis, we tentatively reconstructed their past geographic positions and compared them with the main stages of the margin wedge sequential deformation. The subduction rate of the reliefs (V_r) equals the inter-plate shortening rate ($V_{gps} = 4.7$ cm/yr) minus the shortening rate of the margin wedge (V_s). Quaternary coastal uplift rates were shown to represent ∼4%–8% of the modeled inter-seismic uplift rates in Northern Chili (Jolivet et al., 2020). As shortening and uplift are related in our study zone, V_s could similarly be considered one order of magnitude lower than V_{gps}. V_s sums up the horizontal tectonic shortening estimated from the seismically imaged structures, and diffuse strain caused by pervasive small-scale faulting, loss of porosity and ductile deformation (Adam et al., 2004). With the exception of a few thrust faults at the toe of the margin, no major thrust fault was imaged deforming the margin wedge since ∼0.79 Ma in the promontory area (Figure 2). In contrast, some seismic sections allow estimating that permanent folding across the shelf promontory has accommodated ∼550–∼900 m of shortening since ∼0.712 Ma providing a 0.08–0.12 cm/yr shortening rate (i.e., ∼1.7%–2.6% of V_{gps}). Since diffuse strain, which is assumed to be ∼5%–10% in deformed sediment of the Cascadia frontal accretionary wedge (Adam et al., 2004), is unknown in the fractured basement of Ecuador, and that tectonic shortening by faulting and folding is estimated in the order of 2%–3%, we consider V_s to be at most 10% $V_{gps} = 0.47$ cm/yr implying $V_r = V_{gps} - V_s = 4.23$ cm/yr. This rate is used to calculate the position of the center of the two reliefs at several ages along a time line trending N83°E (Figure 13).

Because these time-related positions were obtained independently of the ages of unconformities Ua, Ub, and Uc, the kinematic model in Figure 13 is considered significant within the limits of the uncertainties on both V_s and the sequential stratigraphy. In this model, relief J underthrusts the outer wedge at ∼1.8 Ma, rising the inter-plate coupling locally, thus contributing to blocking the BJ Fault system. At ∼1 Ma, both reliefs J and CP underthrust the margin wedge increasing the margin normal stress and inter-plate coupling along the entire corridor, uplifting the shelf promontory and freezing the BJ fault system. Between 0.8 and 0.6 Ma, the in-sequence subduction of relief CP and of a speculated saddle between reliefs J and CP, could account for the short subsidence period (∼790–712 ka) of the shelf promontory, followed by its renewed uplift from ∼712 ka. In this scenario, the ∼100 m-thick, upper Early Pleistocene marine to fluvial deposits exposed along the coast west of Jama city (Cantalamessa et al., 2005) would have started uplifting after ∼1 Ma with a ∼0.1 mm/yr mean uplift rate. Additionally, the morphologic scar left in the outer wedge would have formed from ∼790 ka, on the trailing flank of relief CP according to models by Dominguez et al. (2000).

5.3.3. Effect on the Mw 7.8 2016 Earthquake Rupture

Our kinematic model is consistent with the subduction in a row of two reliefs, of which relief CP is buried at a ∼10–15 km depth beneath a faulted margin wedge, and relief J at a ∼25 km-depth in a higher-stress environment. The latter is supported by the high and localized moment released at the J relief during the Mw 7.8, 2016 earthquake (Nocquet et al., 2017). The J relief did not trigger the event, which initiated farther north, nor did it fully stop the southerly spread of the rupture, since a ∼1–2 m co-seismic slip (Gombert et al., 2018; Nocquet et al., 2017) propagated over a ∼25–30-km distance south of the presumed location of relief J. Although the shape and size of relief J are unknown, the earthquake rupture segment boundary could be dominantly controlled by the major along-strike change of the margin basement seismic properties documented by Lynner et al. (2020).

In contrast with the stick-slip frictional instability at relief J, the large 2016-after slip at relief CP (Figure 12) testifies to the up-dip damping of the rupture propagation, which prevented unzipping the whole megathrust up to the trench. The damping reflects either a weak accumulation of stress in that area because of the recurrent SSEs (Rolandone et al., 2018) or a decrease in rigidity of the lower part of the margin (Sallares & Ranero, 2019), or a combination of both. At a ∼10–15-km-depth, relief CP underthrusts basement rocks with ∼5.5 km/s V_p velocity, a value lower than the 6.5 km/s of the margin rocks at 20–25 km depth near relief J (Profile 7, Figure 7 in León-Ríos et al. (2021). Such V_p drop supports a reduced rigidity of the foundation of the margin wedge above relief CP. Fluid circulation associated with increased fracturing related to past subduction of other reliefs could be responsible for the loss of rigidity. Besides, a weak subduction channel and a fluid-driven damage of the underside of the margin's mafic basement (Sage et al., 2006) might contribute to reducing both the margin-basement rigidity and inter-plate friction, thus preventing seismic rupture. In the context of subducted relief CP, this inference looks compatible with global studies stating that rough subducting seafloor is associated with weaker plate coupling and is less prone to nucleate large earthquakes than smooth subduction interface (Lallemand et al., 2018; van Rijsingen et al., 2018). Yet, at relief CP, the margin rigidity seems to remain high enough for the irregular

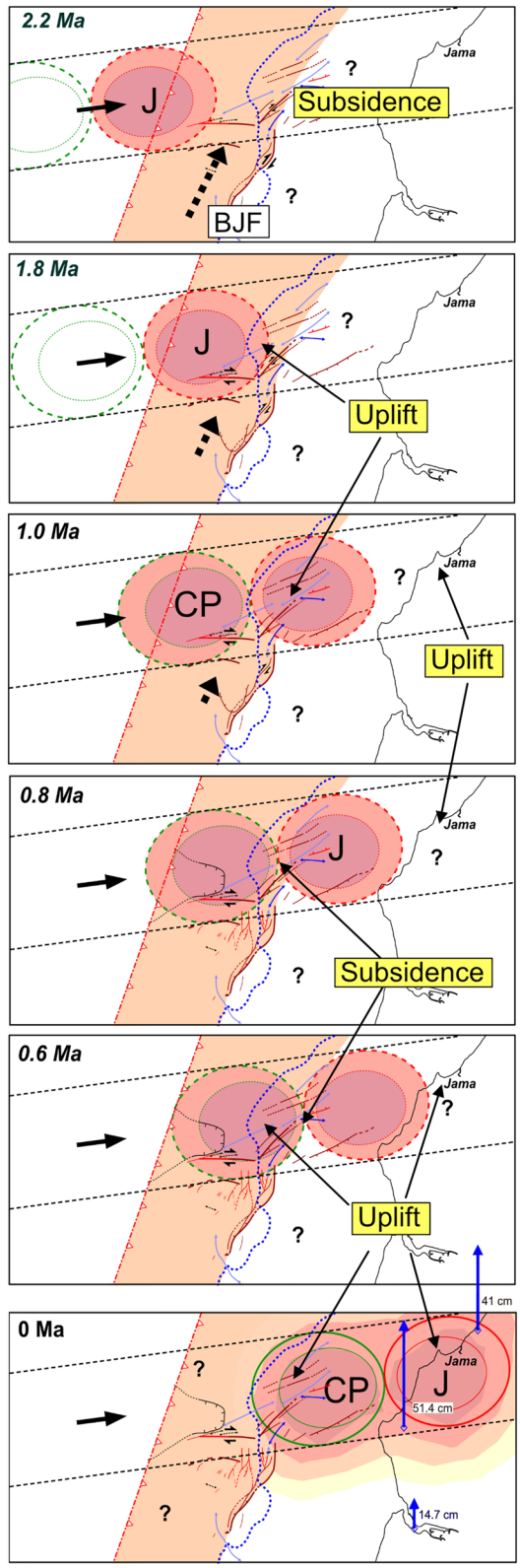
2.2 Ma
J
Subsidence
BJF
Jama
1.8 Ma
J
Uplift
1.0 Ma
CP
Uplift
0.8 Ma
J
Subsidence
0.6 Ma
Uplift
0 Ma
CP
J
41 cm
51.4 cm
14.7 cm

Figure 13.

geometry of the megathrust to resist shear motion, accumulate some elastic strain and hold locked the CP patch, until it fails during episodic SSEs or after-slip. In this view, the CP relief and physical properties of adjacent rocks could have impeded the generation of a significant tsunami during the Mw 7.8, 2016 earthquake. This interpretation, which seems relevant for the mafic, nonaccretionary convergent margin of central Ecuador, contrasts with the proposal that shallow SSE sources are conducive to tsunami earthquakes, especially when the sources are associated with subducted seamounts as suggested on the Hikurangi accretionary margin (Bell et al., 2014; Wallace et al., 2016). However, although no historical tsunami earthquakes are known offshore CP, it is possible that the shallow megathrust has not accumulated enough elastic strain so far, but that it might do so in the future and produce a tsunami, as was the case in Chili during the Mw 8.3, 2015 Illapel earthquake (Melgar et al., 2016).

5.4. A Change in the Mode of Permanent Deformation

Co-seismic surface ruptures preserved in the seafloor topography result from the inelastic part of the deformation, as exemplified by Tsuji et al. (2013) about the rupture of the 2011 Tohoku-oki earthquake. In the study area, part of the permanent deformation of the margin's wedge was likely acquired during large earthquakes, prior to 1.8 and up to 0.79 Ma when segments of the BJF were active, as supported by: (a) well-preserved paleo-seafloor ruptures across the major faults (Figures 4, 7 and 10), and (b) the ∼75 m-thick MTD and its sharp 50-55-m-high vertical offset that presumably reflect repeated ruptures along the NBJ Fault segment (Figure 7).

In contrast, as indicated by seismic reflection data, neither the Mw 8.6–8.8, 1906, and Mw 7.8, 1942 megathrust earthquakes nor the Mw ∼ 7, 1896, 1956, and 1998 thrust earthquakes that occurred astride the creeping barrier (Font et al., 2013; Vaca et al., 2019) were able to reactivate the BJ and Cabuyal fault systems to transfer detectable slip to the seafloor. Rather, post-0.79 Ma shelf promontory deformation appears to have been controlled by gentle folding, and secondary faulting as expressed by (a) the growth of San Vicente and CP anticlines, which is documented at least until ∼130 ka, and (b) the activation of branching faults A4–A5 and the North Canoa Fault documented up to ∼14 ka and possibly to present, based on seafloor morphology (Figures 5, 8, and S5 in Supporting Information S1). These observations mean that the stress field and inter-plate behavior changed at some point from 0.79 Ma, inducing a remarkable modification of the permanent deformation process.

Although multiple mechanisms occurring either deep or shallow along the plate interface could contribute to the permanent deformation as discussed by Melnick (2016) about the central Andean coast, transient aseismic slips and moderate size earthquakes might be the main drivers of the post 0.79 Ma permanent deformation in the study aera. The inter-seismic seismicity (Vaca et al., 2019), the SSEs (Rolandone et al., 2018), the 2016-after-slip and after-shocks sequence (Agurto-Detzel et al., 2019; Rolandone et al., 2018; Soto-Cordero et al., 2020) contribute to multiple faults activation and potentially to the fold growth. The 2016 after-shocks include earthquakes thought to rupture the same seismic asperity repeatedly. Chalumeau et al. (2021) found the repeating earthquakes to cluster near the plate interface. There, the alignment of repeaters-broken seismic asperities along a slightly curved EW-direction (Figure 12) might reflect inter-plate structural complexities related to the northern flank of the subducted CP relief. The modest ∼M3.0 of the repeaters (Chalumeau et al., 2021) and the Mw 3.2–6.0 of the thrust events (Figure 12) (Agurto-Detzel et al., 2019; Rolandone et al., 2018) (Figure 12) imply a moderate off-fault deformation however. Interestingly, 10 weeks after the 2016 main shock, four Mw 3.6–4.6 earthquakes with strike-slip focal mechanisms happened to cluster at shallow depths (8–14 km) (León-Ríos et al., 2019) along the NCa fault, pointing to its dextral reactivation (Figure 12). The fault rupture likely responded to the subduction of relief CP according to the fault network model around a subducted seamount by Dominguez et al. (2000). In addition to this recent fault reactivation, evidence of MTDs emplaced immediately south of the NCa fault (Figure S5 in Supporting Information S1), indicates that roughly ∼712–621 ka ago, the region of the NCa fault suffered from the brunt of earthquakes. Hence, the long-term reactivation of the NCa fault contributed to accumulating

Figure 13. Time-calibrated sketch of the subduction of two reliefs of the Carnegie Ridge (CR) crest hypothesized to be related to the Cabo Pasado (CP) and Jama (J) inter-plate locked asperities. The sketch accounts for the timing of major unconformities Ua (0.79 Ma), Ub (1.0 Ma) and Uc (1.8 Ma) and the successive main stages of margin wedge uplift and subsidence (see Figure 3 for tectonic pattern; dashed blue line is the present shelf edge). (i) Prior to ∼1.8 Ma, an outer-wedge inter-plate coupling (pale orange trench-parallel strip) is necessary to produce outer-wedge strain partitioning (black dashed arrow) and activate the BJ strike-slip faulting (BJF). (ii) Between 1.8 and 1.0 Ma, the subduction of the CR crest reliefs increases locally the inter-plate coupling (dark orange ellipses), blocking progressively the BJ fault system, and uplifting the shelf promontory area. (iii) Between 0.8 and 0.6 Ma, the subduction of an inferred topographic saddle between the "J" and "CP" reliefs leads to a local subsidence, followed by the uplift of the shelf promontory due to the CP relief subduction. Uplift of marine inner-shelf to continental deposits near the city of Jama occurred from ∼1 Ma (Cantalamessa et al., 2005). (iv) 0 Ma, although weaker than at the present-day CP an J locked asperities, an outer-wedge inter-plate coupling may still operate. Vertical blue arrows are 2016-co-seismic uplift in cm (Nocquet et al., 2017).

permanent deformation and shape the Canoa ridge. Thus, we suggest that since the sealing of the BJ and Cabuyal fault system, permanent deformation accumulated primarily during the inter- and post- seismic periods, a similar situation as that proposed by Victor et al. (2011) at the Mejillones Peninsula in Chili.

6. Conclusions

The Quaternary tectonic evolution of the nonaccretionary margin of Ecuador, offshore CP shows that permanent fore-arc deformation resulted from an episode of strike-slip tectonics followed by periods of severe shortening and uplift of the CP shelf promontory. This evolution likely reflects a long-term, inter-plate coupling progression beneath the shelf promontory. The coupling progression was marked by a drastic change in the mode of permanent deformation from co-seismic deformation likely acquired during large earthquakes prior to 1.8 and up to 0.79 Ma when the BJ system was active, to folding and secondary faulting occurring during the post and inter-seismic periods since ∼0.79 Ma. This finding suggests a major change in inter-plate mechanical behavior from a stick-slip mode for several hundred thousand years to a transient aseismic slip mode of similar duration.

The NNE ward translation of an outer-wedge tectonic sliver along the BJ trench parallel, strike-slip fault system prior to ∼1.8 Ma implies that the megathrust was coupled beneath the outer-wedge sliver. Within this view, active strike-slip faults might be regarded as good evidence of significant near-trench coupling at nonaccretionary margins. This hypothesis might be tested in the future as sea-floor geodesy experiments will provide new constraints on the near-trench inter-seismic coupling.

The plate coupling increased strongly beneath the shelf promontory ∼1.8 Ma ago, likely in response to the subduction in a row of J (Jama) and CP reliefs of the CR crest. After a short, period of subsidence, this regime persisted until today in the form of the J and CP geodetically locked patches. An implication of this finding is that the irregular geometry of the subducting reliefs resisting shear motion plays a dominant role in the long- and short-term plate coupling, at least for non-accretionary convergent margins.

In contrast with the J geodetically locked patch, which ruptured seismically during the M7.8, 2016 event, the shallower CP locked patch was the locus of aseismic slip, and is considered associated to a relatively weak megathrust segment. We suggest that the deepest subducted relief J contributed to concentrating high-stress where the highest seismic moment was released during the 2016 earthquake. Unlike, the shallowest relief CP had focused less stress due to a combination of frequent SSEs and a reduced rigidity of the fractured outer-wedge basement, thus impeding updip propagation of the rupture, and hence avoiding the triggering of a significant tsunami during the 2016 event. Therefore, at non-accretionary convergent margins, shallow subducted relief might be considered a natural obstacle to the formation of devastating tsunamis.

Overall, although it is essential to document the ISC coupling by geodesy, and critical to investigate the physical conditions of the plate interface and adjacent rocks, the Quaternary geological evolution of subduction margins provides additional constraints for understanding the current inter-plate coupling and rupture processes.

Data Availability Statement

All data from the Atacames cruise used in this work are available at the French National Marine Database SISMER following the link https://doi.org/10.17600/12010010 (pages are in French and in English). This includes seismic data stored under the folder “Data Managed By SISMER” and « National Bank of Raw Marine Seismic Data ». The first set of files are Chirp data, followed down the list by HR Seismic data. Seismic line number used in this publication refers to the one used in the seismic data base. Data labeled « restricted access » will be made available following a request via an Application Form on the platform after advice of the cruise supervisor conformably to the European and French legislation. Requirement for SCAN-2009 seismic data can be addressed to Dirección de Análisis de Información Estratégica de Hidrocarburos Av República de El Salvador N36-64 y Suecia, Quito 170505. Edificio Ministerio de Energia y Minas. Piso 1, Ecuador.

Acknowledgments
This work was carried out in the frame of the Joint French-Ecuador Laboratory "Earthquakes and Volcanoes in the Northern Andes" and was funded by the Institut de Recherche pour le Développement (IRD), the Institut National des Sciences de l'Univers (INSU), and the Institut Français pour l'Exploitation de la Mer (IFREMER), which provided ship time, equipment, and data processing during the Atacames cruise. We are grateful to the Secretaria de Hydrocarburos del Ecuador (SHE) for providing us with seismic sections from the SCAN-2009 seismic experiment within the framework of the SHE-IRD and SHE-EPN cooperation agreements. We thank Schlumberger for offering the use of Petrel™ software. Finally, we acknowledge two anonymous reviewers and the Associate Editor for their helpful comments.

References

Adam, J., Klaeschen, D., Kukowski, N., & Flueh, E. R. (2004). Upward delamination of Cascadia Basin sediment infill with landward frontal accretion thrusting caused by rapid glacial age material flux. *Tectonics*, *23*(TC3009). https://doi.org/10.1029/2002TC001475

Agurto-Detzel, H., Font, Y., Charvis, P., Régnier, M., Rietbrock, A., Ambrois, D., et al. (2019). Ridge subduction and afterslip control aftershock distribution of the 2016 Mw 7.8 Ecuador earthquake. *Earth and Planetary Science Letters*, *530*, 63–76. https://doi.org/10.1016/j.epsl.2019.05.029

Allmendinger, R. W., Smalley, J. R., Bevis, M., Caprio, H., & Brooks, B. (2005). Bending the Bolivian Orocline in real time. *Geology*, *33*(11), 905–908. https://doi.org/10.1130/G21779.1

Baker, A., Allmendinger, R. W., Owen, L. A., & Rech, J. A. (2013). Permanent deformation caused by subduction earthquakes in northern Chile. *Nature Geoscience*, *6*, 10–1038. https://doi.org/10.1038/NGEO1789

Baldock, J. W. (1983). The northern Andes: A review of the Ecuadorian Pacific margin. In A. E. Nairn, F. G. Stehli, & S. Uyeda (Eds.), *The ocean basins and margins - The pacific ocean* (pp. 181–217). Plenum Press.

Bassett, D., & Watts, A. B. (2015). Gravity anomalies, crustal structure, and seismicity at subduction zones: 1. Seafloor roughness and subducting relief. *Geochemistry, Geophysics, Geosystems*, *16*(5), 1508–1540. https://doi.org/10.1002/2014GC005684

Beck, M. E. (1983). On the mechanism of tectonic transport in zones of oblique subduction. *Tectonophysics*, *93*(1–2), 1–11. https://doi.org/10.1016/0040-1951(83)90230-5

Beck, M. E., Rojas, C., & Cembranos, J. (1993). On the nature of buttressing in margin-parallel strike-slip fault systems. *Geology*, *21*(8), 755–758. https://doi.org/10.1130/0091-7613(1993)021<0755:otnobi>2.3.co;2

Beck, S. L., & Ruff, L. J. (1984). The rupture process of the great 1979 Colombia earthquake: Evidence for the asperity model. *Journal of Geophysical Research*, *89*(B11), 9281–9291. https://doi.org/10.1029/jb089ib11p09281

Béjar-Pizarro, M., Socquet, A., Armijo, R., Carrizo, D., Genrich, J., & Simons, M. (2013). Andean structural control on interseismic coupling in the North Chile subduction zone. *Nature Geoscience*, *6*(6), 462–467. https://doi.org/10.1038/NGEO1802

Bell, R., Holden, C., Power, W., Wang, X., & Downes, G. (2014). Hikurangi margin tsunami earthquake generated by slow seismic rupture over a subducted seamount. *Earth and Planetary Science Letters*, *397*, 1–9. https://doi.org/10.1016/j.epsl.2014.04.005

Berglar, K., Gaedicke, C., Lutz, R., Franke, D., & Djajadihardja, Y. S. (2008). Neogene subsidence and stratigraphy of the Simeulue forearc basin, Northwest Sumatra. *Marine Geology*, *253*(1–2), 1–13. https://doi.org/10.1016/j.margeo.2008.04.006

Bilek, S. L., & Lay, T. (2018). Subduction zone megathrust earthquakes. *Geosphere*, *14*(4), 1468–1500. https://doi.org/10.1130/GES01608.1

Cantalamessa, G., Di Celma, C., & Ragaini, L. (2005). Sequence stratigraphy of the Punta Ballena Member of the Jama formation (Early Pleistocene, Ecuador): Insights from integrated sedimentologic, taphonomic and paleoecologic analysis of molluscan shell concentrations. *Palaeogeography, Palaeoclimatology, Palaeoecology*, *216*(1–2), 1–25. https://doi.org/10.1016/j.palaeo.2004.09.012

Chalumeau, C., Agurto-Detzel, H., De Barros, L., Charvis, P., Galve, A., Rietbrock, A., et al. (2021). Repeating earthquakes at the edge of the afterslip of the 2016 Ecuadorian MW 7.8 Pedernales earthquake. *Journal of Geophysical Research: Solid Earth*, *126*(5), e2021JB021746. https://doi.org/10.1029/2021JB021746

Chemenda, A., Lallemand, S., & Bokun, A. (2000). Strain partitioning and interplate friction in oblique subduction zones: Constraints provided by physical modeling. *Journal of Geophysical Research*, *105*(3), 5567–5582. https://doi.org/10.1029/1999jb900332

Chlieh, M., Mothes, P. A., Nocquet, J.-M., Jarrin, P., Charvis, P., Cisneros, D., et al. (2014). In *Distribution of discrete seismic asperities and aseismic slip along the Ecuadorian Megathrust*. In *Earth and planetary science letters* (Vol. 400, pp. 292–301). https://doi.org/10.1016/j.epsl.2014.05.027

Collot, J.-Y., Marcaillou, B., Sage, F., Michaud, F., Agudelo, W., Charvis, P., et al. (2004). Are rupture zone limits of great subduction earthquakes controlled by upper plate structures?: Evidence from multichannel seismic reflection data acquired across the northern Ecuador - Southwest Colombia margin. *Journal of Geophysical Research*, *109*(B11), 1–14. https://doi.org/10.1029/2004JB003060

Collot, J.-Y., Migeon, S., Spence, G., Legonidec, Y., Marcaillou, B., Schneider, J.-L., et al. (2005). Seafloor margin map helps in understanding subduction earthquakes. *EOS Transactions, American Geophysical Union*, *86*(46), 464–466. https://doi.org/10.1029/2005eo460003

Collot, J. Y., Sanclemente, E., Nocquet, J. M., Leprêtre, A., Ribodetti, A., Jarrin, P., et al. (2017). Subducted oceanic relief locks the shallow megathrust in central Ecuador. *Journal of Geophysical Research: Solid Earth*, *122*(5), 3286–3305. https://doi.org/10.1002/2016JB013849

Davis, D. M., Suppe, J., & Dahlen, F. A. (1983). Mechanics of fold-and-thrust belts and accretionary wedges. *Journal of Geophysical Research*, *88*(B2), 1153–1172. https://doi.org/10.1029/jb088ib02p01153

Diament, M., Harjono, H., Karta, K., Deplus, C., Dahrin, D., Zen, M. T. J., et al. (1992). In *Mentawai fault zone off Sumatra: A new key to the geodynamics of western Indonesia* (Vol. 20, pp. 259–262).

Dominguez, S., Malavieille, J., & Lallemand, S. (2000). Deformation of margins in response to seamount subduction insights from sandbox experiments. *Tectonics*, *19*, 182–196.

Embry, A. F. (1993). Transgressive-regressive (T–R) sequence analysis of the Jurassic succession of the Sverdrup basin, Canadian Arctic Archipelago. *Canadian Journal of Earth Sciences*, *30*, 301–320.

Fitch, T. J. (1972). Plate convergence, transcurrent faults, and internal deformation adjacent to Southeast Asia and the western Pacific. *Journal of Geophysical Research*, *77*, 4432–4460.

Font, Y., Segovia, M., Vaca, S., & Theunissen, T. (2013). Seismicity patterns along the Ecuadorian subduction zone: New constraints from earthquake location in a 3-D a priori velocity model. *Geophysical Journal International*, *193*(1), 263–286. https://doi.org/10.1093/gji/ggs083

Gagnon, K., Chadwell, C. D., & Norabuena, E. (2005). Measuring the onset of locking in the Peru–Chile trench with GPS and acoustic measurements. *Nature*, *434*(7030), 205–207. https://doi.org/10.1038/nature03412

Goldfinger, C., Nelson, C. H., Morey, A. E., Johnson, J. E., Patton, J. R., Karabanov, E., et al. (2012). Turbidite event history—Methods and implications for Holocene paleoseismicity of the Cascadia subduction zone (Vol. *170*). U. S. Geological Survey, Professional Paper 1661–F, Professional Paper 1661–F. Retrieved from http://pubs.usgs.gov/pp/pp1661/f

Gombert, B., Duputel, Z., Jolivet, R., Simons, M., Jiang, J., Liang, C., et al. (2018). Strain budget of the Ecuador–Colombia subduction zone: A stochastic view. *Earth and Planetary Science Letters*, *498*, 288–299. https://doi.org/10.1016/j.epsl.2018.06.046

Graindorge, D., Calahorrano, A., Charvis, P., Collot, J.-Y., & Bethoux, N. (2004). Deep structures of the Ecuador convergent margin and the Carnegie Ridge, possible consequence on great earthquakes recurrence interval. *Geophysical Research Letters*, *31*(4), L04603. https://doi.org/10.1029/2003GL018803

Gutscher, M. A., Malavieille, J., Lallemand, S., & Collot, J. Y. (1999). Tectonic segmentation of the north Andean margin: Impact of the Carnegie Ridge collision. *Earth and Planetary Science Letters*, *168*(3–4), 255–270. https://doi.org/10.1016/s0012-821x(99)00060-6

Hansen, J., Sato, M., Russell, G., & Kharecha, P. (2013). *Climate sensitivity, sea level and atmospheric carbon dioxide* (Vol. 371). Philosophical Transactions of the Royal Society of London, A. https://doi.org/10.1098/rsta.2012.0294

Hayes, G. P., Wald, D. J., & Johnson, R. L. (2012). Slab1.0: A three-dimensional model of global subduction zone geometries. *Journal of Geophysical Research*, *117*(B01302). https://doi.org/10.1029/2011JB008524

Hernández, M. J., Michaud, F., Collot, J.-Y., Proust, J.-N., & d'Acremont, E. (2020). Evolution of the Ecuador offshore nonaccretionary-type forearc basin and margin segmentation. *Tectonophysics*, *781*, 228374. https://doi.org/10.1016/j.tecto.2020.228374

Jaillard, E., Lapierre, H., Ordoñez, M., Toro Álava, J., Amórtegui, A., & Vanmelle, J. (2009). *Accreted oceanic terranes in Ecuador: Southern edge of the Caribbean plate?* (pp. 489–485). Geological Society, London, Special Publications edited.

Jara-Muñoz, J., Melnick, D., Zambrano, P., Rietbrock, A., González, J., Argandoña, B., & Strecker, M. R. (2017). Quantifying offshore forearc deformation and splay-fault slip using drowned Pleistocene shorelines, Arauco Bay, Chile. *Journal of Geophysical Research: Solid Earth*, *122*(6), 4529–4558. https://doi.org/10.1002/2016JB013339

Jarrard, R. D. (1986b). Relations among subduction parameters. *Reviews of Geophysics*, *24*(2), 217–284. https://doi.org/10.1029/rg024i002p00217

Jarrard, R. D. (1986a). Terrane motion by strike slip faulting of forearc slivers. *Geology*, *14*(9), 780–783. https://doi.org/10.1130/0091-7613(1986)14<780:tmbsfo>2.0.co;2

Jolivet, R., Simons, M., Duputel, Z., Olive, J.-A., Bhat, H. S., & Bletery, Q. (2020). Interseismic loading of subduction megathrust drives long-term uplift in northern Chile. *Geophysical Research Letters*, *47*(8), e2019GL085377. https://doi.org/10.1029/2019GL085377

Kame, N., Rice, J. R., & Dmowska, R. (2003). Effects of prestress state and rupture velocity on dynamic fault branching. *Journal of Geophysical Reasearch*, *108*(B5), 2265. https://doi.org/10.1029/2002JB002189

Kanamori, H., & McNally, K. C. (1982). Variable rupture mode of the subduction zone along the Ecuador-Colombia coast. *Bulletin of the Seismological Society of America*, *72*, 1241–1253.

Kelleher, J. (1972). Rupture zones of large South American earthquakes and some predictions. *Journal of Geophysical Research*, *77*(11), 2087–2103. https://doi.org/10.1029/JB077i011p02087

Koch, C. D., Lynner, C., Delph, J., Beck, S. L., Meltzer, A., Font, Y., et al. (2020). Structure of the Ecuadorian forearc from the joint inversion of receiver functions and ambient noise surface waves. *Geophysical Journal International*, *222*(3), 1671–1685. https://doi.org/10.1093/gji/ggaa237

Lallemand, S., Liu, C.-S., Dominguez, S., Schnurle, P., Malavieille, J., & the ACT Scientific Crew (1999). trench-parallel stretching and folding of forearc basins and lateral migration of the accretionary wedge in the southern Ryukyus: A case of strain partition caused by oblique convergence. *Tectonics*, *18*(2), 231–247. https://doi.org/10.1029/1998tc900011

Lallemand, S., Peyret, M., van Rijsingen, E., Arcay, D., & Heuret, A. (2018). Roughness characteristics of oceanic seafloor prior to subduction in relation to the seismogenic potential of subduction zones. *Geochemistry, Geophysics, Geosystems*, *19*(7), 2121–2146. https://doi.org/10.1029/2018GC007434

Lallemand, S. E., Schnurle, P. S., & Malavieille, J. (1994). Coulomb theory applied to accretionary and non accretionary wedges: Possible causes for tectonic erosion and/or frontal accretion. *Journal of Geophysical Research*, *99*(B6), 12033–012055. https://doi.org/10.1029/94jb00124

León-Ríos, S., Agurto-Detzel, H., Rietbrock, A., Alvarado, A., Beck, S., Charvis, P., et al. (2019). 1D-velocity structure and seismotectonics of the Ecuadorian margin inferred T from the 2016 Mw7.8 Pedernales aftershock sequence. *Journal of Geophysical Research: Solid Earth*, *767*. https://doi.org/10.1016/j.tecto.2019.228165

León-Ríos, S., Bie, L., Agurto-Detzel, H., Galve, A., Alvarado, A., Beck, S., et al. (2021). 3D local earthquake tomography of the Ecuadorian margin in the source area of the 2016 Mw 7.8 Pedernales earthquake. *Journal of Geophysical Research: Solid Earth*, *126*(3). https://doi.org/10.1029/2020JB020701

Liberty, L. M., Brothers, D. S., & Haeussler, P. J. (2019). Tsunamigenic splay faults imply a long-term asperity in southern Prince William Sound, Alaska. *Geophysical Research Letter*. https://doi.org/10.1029/2018GL081528

Lieser, K., Grevemeyer, I., Lange, D., Flueh, E., Tilmann, F., & Contreras-Reyes, E. (2014). Splay fault activity revealed by aftershocks of the 2010 Mw 8.8 Maule earthquake, central Chile. *Geology*, *42*(9), 823–826. https://doi.org/10.1130/G35848.1

Lisiecki, L. E., & Raymo, M. E. (2005). A Pliocene-Pleistocene stack of 57 globally distributed benthic D18O records. *Paleoceanography*, *20*(1). https://doi.org/10.1029/2004PA001071

Lonsdale, P. (1978). Ecuadorian subduction system. *Bulletin - American Association of Petroleum Geologists*, *62*(12), 2454–2477.

Loveless, J. P., & Meade, B. J. (2011). Spatial correlation of interseismic coupling and coseismic rupture extent of the 2011 MW = 9.0 Tohoku-oki earthquake. *Geophysical Research Letters*, *38*(L17306). https://doi.org/10.1029/2011GL048561

Luzieux, L. D. A., Heller, F., Spikings, R., Vallejo, C. F., & Winkler, W. (2006). Origin and Cretaceous tectonic history of the coastal Ecuadorian forearc between 1°N and 3°S: Paleomagnetic, radiometric and fossil evidence. *Earth and Planetary Science Letters*, *249*, 400–414.

Lynner, C., Koch, C., Beck, S. L., Meltzer, A., Soto-Cordero, M., Hoskins, M. C., et al. (2020). Upper-plate structure in Ecuador coincident with the subduction of the Carnegie Ridge and the southern extent of large mega-thrust earthquakes. *Geophysical Journal International*, *220*(3), 1965–1977. https://doi.org/10.1093/gji/ggz558

Mann, P. (2007). Global catalogue, classification and tectonic origins of restraining- and releasing bends on active and ancient strike-slip fault systems. In W. D. Cunningham & P. Mann (Eds.), *Tectonics of strike-slip restraining and releasing bends* (pp. 13–142). Geological Society, London, Special Publications.

Matsuura, M., & Sato, T. (1989). A dislocation model for the earthquake cycle at convergent plate boundaries. *Geophysical Journal*, *96*(1), 23–32. https://doi.org/10.1111/j.1365-246x.1989.tb05247.x

McCaffrey, R. (1992). Oblique plate convergence, slip vectors, and forearc deformation. *Journal of Geophysical Research*, *97*(B6), 8905–908915. https://doi.org/10.1029/92jb00483

McCaffrey, R., Zwick, P. C., Bok, Y., Prawirodirdjo, L., Genrich, J. F., Stevens, C. W., et al. (2000). Strain partitioning during oblique plate convergence in northern Sumatra: Geodetic and seismologic constraints and numerical modeling. *Journal of Geophysical Reasearch*, *105*(B12), 23363–28376.

Melgar, D., Fan, W., Riquelme, S., Geng, J., Liang, C., Fuentes, M., et al. (2016). Slip segmentation and slow rupture to the trench during the 2015, Mw8.3 Illapel, Chile earthquake. *Geophysical Research Letters*, *43*. https://doi.org/10.1002/2015GL067369

Melnick, D. (2016). Rise of the central Andean coast by earthquakes straddling the Moho. *Nature Geoscience*, *9*(5), 10–1038. https://doi.org/10.1038/NGEO2683

Mendoza, C., & Dewey, J. W. (1984). Seismicity associated with the great Colombia-Ecuador earthquakes of 1942, 1958 and 1979: Implications for barrier models of earthquake rupture. *Bulletin of the Seismological Society of America*, *74*(2), 577–593.

Michaud, F., Proust, J. N., Collot, J. Y., Lebrun, J. F., Witt, C., Ratzov, G., et al. (2015). Quaternary sedimentation and active faulting along the Ecuadorian shelf: Preliminary results of the ATACAMES cruise (2012). *Marine Geophysical Researches*, *36*(1), 91–98. https://doi.org/10.1007/s11001-014-9231-y

Miller, K. G., Kominz, M. A., Browning, J. V., Wright, J. D., Mountain, G. S., Katz, G. S., et al. (2005). The Phanerozoic record of global sea-level change. *Science*, *310*, 1293–1298. https://doi.org/10.1126/science.1116412

Moreno, M., Rosenau, M., & Oncken, O. (2010). Maule earthquake slip correlates with pre-seismic locking of Andean subduction zone. *Nature Letters*, *46*(7312), 198–202. https://doi.org/10.1038/nature09349

Nocquet, J.-M., Jarrin, P., Vallée, M., Mothes, P. A., Grandin, R., Rolandone, F., et al. (2017). Supercycle at the Ecuadorian subduction zone revealed after the 2016 Pedernales earthquake. *Nature Geoscience*, *10*(2), 146–149. https://doi.org/10.1038/NGEO2864

Nocquet, J.-M., Villegas-Lanza, J. C., Chlieh, M., Mothes, P. A., Rolandone, F., Jarrin, P., et al. (2014). Motion of continental slivers and creeping subduction in the northern Andes. *Nature Geoscience*, *7*(4), 1–5. https://doi.org/10.1038/NGEO2099

Pennington, W. D. (1981). Subduction of the eastern Panama basin and seismotectonics of northwestern south America. *Journal of Geophysical Research*, *86*(B11), 10753–10770. https://doi.org/10.1029/jb086ib11p10753

Perfettini, H., Avouac, J.-P., Tavera, H., Kositsky, A., Nocquet, J.-M., Bondoux, F., et al. (2010). Seismic and aseismic slip on the Central Peru megathrust. *Nature*, *465*(7294), 78–81. https://doi.org/10.1038/nature09062

Philibosian, B., Sieh, K., Avouac, J.-P., Natawidjaja, D. H., Chiang, H. W., Wu, C.-C., et al. (2014). Rupture and variable coupling behavior of the Mentawai segment of the Sunda megathrust during the supercycle culmination of 1797 to 1833. *Journal of Geophysical Reasearch*, *119*(9), 7258–7287. https://doi.org/10.1002/2014JB011200

Popescu, S.-M. (2021). *Plio-pleistocene foraminifera from Ecuador - biostratigraphy* (pp. 1–19). GeobiostratData Consulting. Retrieved from https://hal.archives-ouvertes.fr/hal-03669503

Proust, J. N., & Chanier, F. (2004). The Pleistocene cape kidnappers section in New Zealand: Orbitally-forced controls on active margin sedimentation. *Journal of Quaternary Science*, *19*(6), 591–603. https://doi.org/10.1002/jqs.865

Proust, J.-N., Martillo, C., Michaud, F., Collot, J.-Y., & Dauteuil, O. (2016). Subduction of seafloor asperities revealed by a detailed stratigraphic analysis of the active margin shelf sediments of Central Ecuador. *Marine Geology*, *380*, 345–362. https://doi.org/10.1016/j.margeo.2016.03.014

Reyes, P., & Michaud, F. (2012). *Mapa Geologico de la Margen Costera Ecuatoriana (1/1500000)*. EPPetroEcuador-IRD Quito.

Rolandone, F., Nocquet, J.-M., Mothes, P. A., Jarrin, P., Vallée, M., Cubas, N., et al. (2018). Areas prone to slow slip events impede earthquake rupture propagation and promote afterslip. *Science Advances*, *4*(1), eaao6596. https://doi.org/10.1126/sciadv.aao6596

Ruh, J. B., Gerya, T., & Burg, J.-P. (2013). High-resolution 3D numerical modeling of thrust wedges: Influence of décollement strength on transfer zones. *Geochemistry, Geophysics, Geosystems*, *14*(4), 1131–1155. https://doi.org/10.1002/ggge.20085

Ruh, J. B., Sallarès, V., Ranero, C. R., & Gerya, T. (2016). Crustal deformation dynamics and stress evolution during seamount subduction: High-resolution 3-D numerical modeling. *Journal of Geophysical Research: Solid Earth*, *121*(9), 6880–6902. https://doi.org/10.1002/2016JB013250

Sage, F., Collot, J.-Y., & Ranero, C. R. (2006). Interplate patchiness and subduction-erosion mechanisms: Evidence from depth migrated seismic images at the Central Ecuador convergent margin. *Geology*, *34*(12), 997–1000. https://doi.org/10.1130/G22790A.1

Saillard, M., Audin, L., Rousset, B., Avouac, J.-P., Chlieh, M., Hall, S. R., & Farber, D. L. (2017). From the seismic cycle to long-term deformation: Linking seismic coupling and quaternary coastal geomorphology along the Andean megathrust. *Tectonics*, *36*(2), 241–256. https://doi.org/10.1002/2016TC004156

Sallares, V., Charvis, P., Flueh, E. R., & Bialas, J., & Scientific Party Salieri. (2005). Seismic structure of the Carnegie Ridge and the nature of the Galàpagos Hotspot. *Geophysical Journal International*, *161*(3), 763–788. https://doi.org/10.1111/j.1365-246x.2005.02592.x

Sallares, V., & Ranero, C. (2019). Upper-plate rigidity determines depth-varying rupture behaviour of megathrust earthquakes. *Nature*, *576*(7785), 96–101. org/. https://doi.org/10.1038/s41586-019-1784-0

Scholz, C. H. (1998). Earthquakes and friction laws. *Nature*, *391*(1), 37–42. https://doi.org/10.1038/34097

Schwartz, S. Y., & Rokosky, J. M. (2007). Slow slip events and seismic tremor at circum-pacific subduction zones. *Reviews of Geophysics*, *45*, RG3004.

Somoza, R., & Ghidella, M. E. (2012). Late Cretaceous to recent plate motions in western South America revisited. *Earth and Planetary Science Letters*, *331–332*, 152–163. https://doi.org/10.1016/j.epsl.2012.03.003

Soto-Cordero, L., Meltzer, A., Bergman, E., Hoskins, M., Stachnik, J. C., Agurto-Detzel, H., et al. (2020). Structural control on megathrust rupture and slip behavior: Insights from the 2016 Mw 7.8 Pedernales Ecuador earthquake: Insights from the 2016 Mw 7.8 Pedernales Ecuador earthquake. *Journal of Geophysical Research: Solid Earth*, *125*(2), e2019JB018001. https://doi.org/10.1029/2019JB018001

Swenson, J. L., & Beck, S. L. (1996). Historical 1942 Ecuador and 1942 Peru subduction earthquakes, and earthquake cycles along Colombia-Ecuador and Peru subduction segments. *Pageoph*, *146*(1), 67–101. https://doi.org/10.1007/bf00876670

ten Brink, U., & Lin, J. (2004). Stress interaction between subduction earthquakes and forearc strike-slip faults: Modeling and application to the northern Caribbean plate boundary. *Journal of Geophysical Reasearch*, *109*(B12), B12310. https://doi.org/10.1029/2004JB003031

Tsuji, T., Kawamura, K., Kanamatsu, T., Kasaya, T., Fujikura, K., Ito, Y., et al. (2013). Extension of continental crust by anelastic deformation during the 2011 Tohoku-oki earthquake: The role of extensional faulting in the generation of a great tsunami. *Earth and Planetary Science Letters*, *364*, 44–58. https://doi.org/10.1016/j.epsl.2012.12.038

Vaca, S., Vallée, M., Nocquet, J.-M., & Alvarado, A. (2019). Active deformation in Ecuador enlightened by a new waveform-based T catalog of earthquake focal mechanisms. *Journal of South American Earth Sciences*, *93*, 449–461. https://doi.org/10.1016/j.jsames.2019.05.017

Vail, P. R., Mitchum, R. M., Jr., & Thompson, S., III. (1977). Seismic stratigraphy and global changes of sea level, part 3: Relative changes of sea level from coastal onlap. In C. E. Payton (Ed.), *American Association of Petroleum Geologists* (pp. 63–81).

van Dinther, Y., Gerya, T. V., Dalguer, L. A., Mai, P. M., Morra, G., & Giardini, D. (2013). The seismic cycle at subduction thrusts: Insights from seismo-thermo-mechanical models. *Journal of Geophysical Research: Solid Earth*, *118*(12), 6183–6202. https://doi.org/10.1002/2013JB010380

van Rijsingen, E., Lallemand, S., Peyret, M., Arcay, D., Heuret, A., Funiciello, F., & Corbi, F. (2018). How subduction interface roughness influences the occurrence of large interplate earthquakes. *Geochemistry, Geophysics, Geosystems*, *19*(8), 1–29. https://doi.org/10.1029/2018GC007618

Victor, P., Sobiesiak, M., Glodny, J., Nielsen, S. N., & Oncken, O. (2011). Long-term persistence of subduction earthquake segment boundaries: Evidence from Mejillones Peninsula, northern Chile. *Journal of Geophysical Reasearch*, *116*(B02402), B02402. https://doi.org/10.1029/2010JB007771

von Huene, R., & Scholl, D. W. (1991). Observations at convergent margins concerning sediment subduction, subduction erosion, and growth of continental crust. *Reviews of Geophysics*, *29*(3), 279–316. https://doi.org/10.1029/91rg00969

Wallace, L. M., Webb, S. C., Ito, Y., Mochizuki, K., Hino, R., Henrys, S., et al. (2016). Slow slip near the trench at the Hikurangi subduction zone, New Zealand. *Science*, *352*(6286), 701–704. https://doi.org/10.1126/science.aaf2349

Wang, K. (1996). Simplified Analysis of horizontal stresses in a buttressed forearc sliver at an oblique subduction zone. *Geophysical Research Letters*, *23*(16), 2021–2024. https://doi.org/10.1029/96gl02067

Wang, K. (2010). Finding fault in fault zones. *Science*, *329*, 152–153. https://doi.org/10.1126/science.1192223

Wang, K., & Bilek, S. L. (2014). Invited review paper: Fault creep caused by subduction of rough seafloor relief. *Tectonophysics*, *610*, 1–24. https://doi.org/10.1016/j.tecto.2013.11.024

Wang, K., & Dixon, T. (2004). Coupling" semantics and science in earthquake Research. *EOS Transactions, American Geophysical Union*, *85*(18), 179–180. https://doi.org/10.1029/2004eo180005

Wang, K., & Hu, Y. (2006). Accretionary prisms in subduction earthquake cycles: The theory of dynamic Coulomb wedge. *Journal of Geophysical Research*, *111*(B06410). https://doi.org/10.1029/2005JB004094

Wessel, P., & Smith, W. D. (1998). New, improved version of generic mapping tools released. *EOS Transactions, American Geophysical Union*, *79*(47), 579. https://doi.org/10.1029/98eo00426

Yamaguchi, A., Sakaguchi, A., Sakamoto, T., Iijima, K., Kameda, J., Kimura, G., et al. (2011). Progressive illitization in fault gouge caused by seismic slip propagation along a megasplay fault in the Nankai Trough. *Geology*, *39*(11), 995–998. https://doi.org/10.1130/G32038.1

Ye, A., Kanamori, H., Avouac, J.-P., Li, L., Fai Cheung, K., & Lay, T. (2016). The 16 April 2016, MW7.8(MS7.5) Ecuador earthquake. *Earth and Planetary Science Letters*, *454*, 248–258. https://doi.org/10.1016/j.epsl.2016.09.006

Yilmaz, O. (2001). Seismic data analysis. In *Processing, inversion and interpretation of seismic data*, (p. 2065). Society of Exploration Geophysicist.

Yokota, Y., Ishikawa, T., Watanabe, S.-i., Tashiro, T., & Asada, A. (2016). Seafloor geodetic constraints on interplate coupling of the Nankai Trough megathrust zone. *Nature*, *534*(7607), 374–377. https://doi.org/10.1038/nature17632